ALL INKJET-PRINTED HIGH ON/OFF RATIO TWO-DIMENSIONAL MATERIALS FIELD EFFECT TRANSISTOR

by

Mohi Uddin Jewel, B.Sc.

A thesis submitted to the Graduate Council of
Texas State University in partial fulfillment
of the requirements for the degree of
Master of Science
with a Major in Engineering
August 2018

Committee Members:

Maggie Yihong Chen, Chair

Ravi Droopad

Qingkai Yu

COPYRIGHT

by

Mohi Uddin Jewel

2018

FAIR USE AND AUTHOR'S PERMISSION STATEMENT

Fair Use

Duplication Permission

ACKNOWLEDGEMENTS

I would like to acknowledge the support and guidance of Dr. Maggie Yihong Chen toward the successful completion of this work. I will always remember those countless hours she spent with me in the interpreting theoretical aspects, experimental data, or just offering words of wisdom. I would also thank Dr. Ravi Droopad for his careful review of this work and scholarly discussion. I would like to thank Dr. Qingkai Yu for being an active member of my thesis committee and his insightful comments over the course of this thesis. This project was financially supported by the grant from NASA STTR Phase II under contract no. NNX15CC34C, and I would like to acknowledge them. I would like to thank my fellow lab mate Mahmuda Akter Monne for solving various theoretical problems and helpful group discussions. Finally, I want to thank my parents, brothers, and sister for their unconditional love and support for me.

TABLE OF CONTENTS

Page

LIST OF TABLES

Table **Page**

LIST OF FIGURES

Figure **Page**

ABSTRACT

This thesis introduces the development of a novel ink, design, fabrication, and characterization of an all inkjet printed high current on/off ratio field effect transistor (FET). The inks were obtained through the liquid phase exfoliation of nitrogen-doped graphene (NDG), and molybdenum disulfide (MoS_2) nanosheets into appropriate solvents. A stable and efficient method of inkjet printing is developed for NDG nanosheets. The concentration of nanosheets and the presence of MoS_2 were determined from UV-Vis spectra of the inks. The morphology of percolation clusters using NDG was studied using the thickness profile and scanning electron microscopy (SEM) images. The solvent-induced defects in NDG nanosheets were characterized by Raman spectroscopy. There were little or no solvent-induced defects in the nanosheets recovered by curing after printing. Barium titanate ($BaTiO_3$) was prepared and used as a high *k (~20.5)* dielectric for the printed transistors. The NDG transistors were designed, fabricated, and characterized on the glass substrate. Due to the low on/off ratio of NDG transistors, NDG thin films were electrochemically doped with MoS_2 by multiple printing passes. The incorporation of semiconducting MoS_2 into NDG was confirmed by energy dispersive spectroscopy (EDS) for further analysis. A transistor with high current on/off ratio was obtained by NDG-MoS_2 heterostructures channel. To our best knowledge, this is the highest on/off ratio for a fully inkjet printed transistor based on 2D materials.

I. INTRODUCTION

1.1. Introduction

Modern civilization has largely been shaped by the applications of electronics. Over the last half-century, electronics have revolutionized our daily life. With the unprecedented advancement in silicon and compound semiconductor technology, electronic products such as computers, mobile phones, televisions, camera have become ubiquitous. Modern processors are made of billions of transistors which enable faster computations with less power use. Microcontroller based solutions enable sensor-based technology for portable devices to large stationary installations. Solar energy from photovoltaic cells is increasingly getting dominance in the renewable energy market. Light emitting diodes (LEDs) are being widely used. For example, light bulbs and liquid crystal displays (LCDs) are getting replaced by LEDs and LED displays. One limitation of traditional semiconductors such as silicon, germanium, and gallium arsenide, is that they are rigid and cannot be used for flexible electronics [1].

Yet, another revolution is taking place in the field of flexible electronics. Flexible electronics have a rapidly growing market, and the market for wearable technology is expected to grow over $34 billion in 2020 [2]. Several applications of flexible electronics such as organic light emitting diodes (OLEDs), photovoltaic devices, and flexible displays are now in the market [3,4]. Presently, an extensive research is going on to develop flexible transistors, sensors, memory devices, and electronic textiles [5,6,7]. Flexible device development mainly relies on two fabrication techniques: one is transfer printing, another one is silicon microfabrication technique [8]. Both these methods require many fabrication steps for a complete device fabrication and are costly.

Therefore, a new technology for flexible electronics is required to reduce the number of process-steps compared to conventional silicon microfabrication technique and be compatible with flexible substrates. Printed electronics have the potential to fulfill these requirement [9]. Inkjet printing as a process for printed electronics, has become more popular for the fabrication of electronic devices because of its ability for large-area fabrication, an involvement of the limited number of process steps, low-temperature processing, and low cost. Inkjet printing is a widely used technique to print texts and graphics. With some modifications, it has become a well-established technique to print conducting, semiconducting, and insulating materials of given patterns to fabricate electronic devices. [10]. It is also possible to achieve layer-by-layer printing with different thickness and different structures in every layer, which is why we plan to use this 3D inkjet printing technique. However, inkjet printed two dimensional (2D) materials-based transistors exhibit low current on/off ratio which is addressed in this research.

This thesis introduces the development of a novel ink, design, fabrication, and characterization of an all inkjet printed high current on/off ratio field effect transistor (FET). The inks were obtained through the liquid phase exfoliation of nitrogen-doped graphene (N-graphene) and molybdenum disulfide (MoS_2) nanosheets into appropriate solvents. The ability to generate droplets of that printable inks have been analyzed by their viscosity, surface tension, density, and droplet kinetics. The concentration of nanosheets and the presence of MoS_2 were determined from UV-Vis spectra of the inks. The morphology of percolation clusters using NDG was studied using the thickness profile and scanning electron microscopy (SEM) images. The solvent-induced defects in

NDG nanosheets were characterized by Raman spectroscopy. There were little or no solvent-induced defects in the nanosheets recovered by curing after printing. Barium titanate ($BaTiO_3$) was prepared and used as a high *k (~20.5)* dielectric for the printed transistors. The NDG transistors were designed, fabricated, and characterized on the glass substrate. Due to the low current on/off ratio of NDG transistors, NDG thin films were electrochemically doped with MoS_2 by multiple printing passes. A transistor with high current on/off ratio was obtained with NDG-MoS_2 percolation cluster channel. The incorporation of semiconducting MoS_2 into NDG was confirmed by energy dispersive spectroscopy (EDS) for further analysis. To our best knowledge, this is the highest on/off ratio for a 100% inkjet printed transistor based on 2D materials.

The following sections contain the historic background of the printing technology, overview of Fujifilm Dimatix printer (DMP 2800), inkjet printed devices, and inkjet printed transistors. Finally, the framework of the thesis is established.

1.2. Background

The conventional process takes several steps to develop a film pattern on a substrate such as thin film deposition, photoresist coat, bake, pattern transfer through UV-light exposure, developer use, etch, and rinse. However, printing is an additive deposition in which the thin film pattern is printed and baked to develop the pattern on a substrate. There are several printing processes for printed electronics. They are i) Roll-to-Roll printing, ii) Gravure printing, iii) Screen printing, iv) Flexographic printing, v) Inkjet and aerosol jet printing, vi) Transfer printing, vii) Nanoimprinting, and viii) Spray coating. Jet printing has several advantages, such as a variable digital pattern, on-the-fly error correction, non-contact printing, low operation cost, and availability of wide range

of inks. Jet printings are used in electronics devices, interconnects, RF antennas, LCD spacers, and Polyimide alignment layers. Inkjet printing was employed in this research which will be discussed in the subsequent sections.

1.3. Inkjet Printing Technology

Inkjet printing technology is divided into two categories, based on the mechanism of droplet generation. They are continuous and drop-on-demand (DOD) inkjet printing technology [11]. In continuous inkjet printers (CIJs), a continuous stream of ink is created by pushing the liquid ink through a gun body and microscopic nozzle via a high-pressure pump. A piezoelectric crystal pulse is used to break the inkjet into droplets inside the chamber. Some of the droplets in this stream are electrostatically charged. These charged droplets are passing through a deflecting electrode and their deflection depend on their charge. The charged droplets are used to print the pattern onto the paper. The uncharged droplets are collected in the gutter and fed back into the ink circuit.

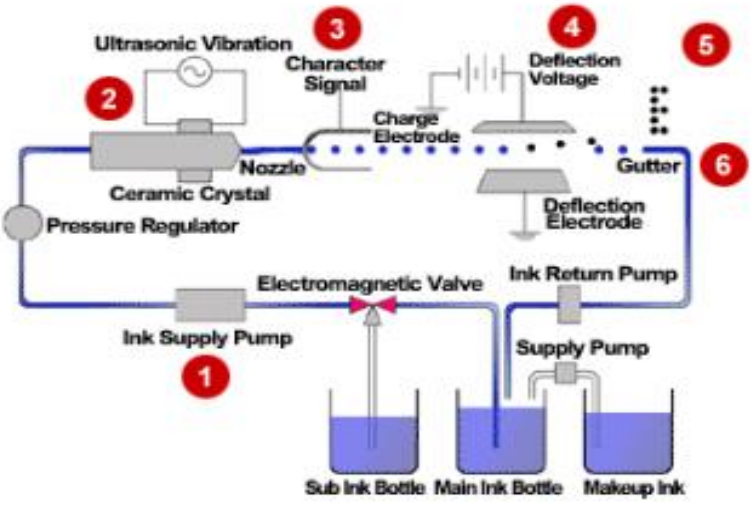

Figure 1. A continuous ink-jet system [This image is copyrighted by Hitachi America Ltd.]

Today, most of the inkjet printers use drop-on-demand printing process. The DOD

printing is further classified into three sorts, depending on the pulse generation process, namely thermal, piezo, and electrostatic inkjet. The DOD process provides a small volume of liquid (picolitre) with high positional accuracy, high speed, and low cost. Inkjet printers mainly use two different nozzle technologies: thermal bubble jets and piezoelectric jets. Thermal inkjet printers use the current pulse to heat the ink. The ink is stored in an ink reservoir and a current pulse through the heating element vaporizes the ink nearby printhead. Bubbles form, expand, and the internal pressure ejects out the ink into a droplet. The total ejection takes a few microseconds. The heating element is made of poly-silicon, and cheaper to manufacture.

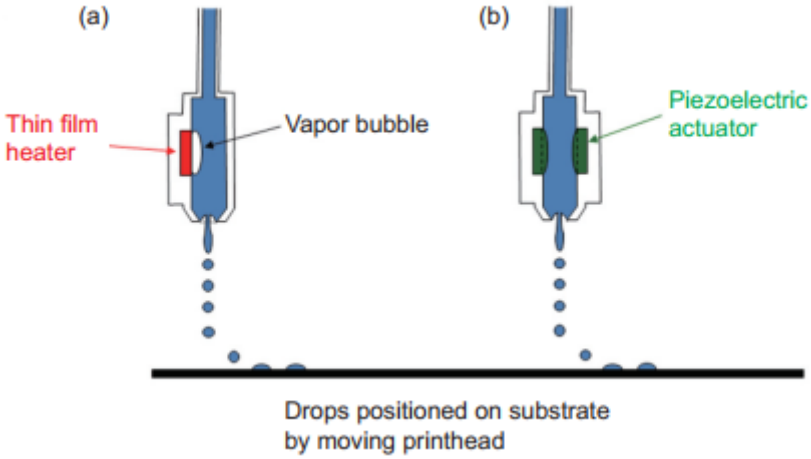

Figure 2. Schematic of a drop-on-demand inkjet printer (DOD) with (a) thermal and (b) piezoelectric actuation [12].

Piezoelectric inkjet printers use a piezoelectric plate to eject the ink through the nozzles. A voltage pulse is applied to the piezoelectric transducer (PZT) to eject the droplets. An acoustic wave propagates inside the ink chamber due to the PZT actuation. This acoustic wave causes the ejection of droplets from an inkjet. Total actuation time for PZT transducer is a few microseconds, which is faster than thermal inkjet printers because PZT transducer does not require extra time for cooling. Due to no thermal stress

in the ink, multiple inks can be printed using a piezoelectric printer. In this thesis, all inkjet printings were performed using Fujifilm Dimatix Inkjet (DMP 2800) printer which used piezoelectric transducers. The details of Fujifilm printer will be discussed in the next section.

1.3.1. Fujifilm Dimatix (DMP 2800) Printer

The Fujifilm Dimax (DMP 2800) is a commercial piezoelectric inkjet printer. Figure 3a shows the Fujifilm Dimatix materials printer. It has a chamber which has a platen for a letter-size substrate, drop watcher module and print carriage assembly. The stage motor has a 5 μm resolution. The substrate can be heated up to 60 ^{o}C. The nozzle temperature can increase during printing because of the substrate heating, which evaporates solvents when the inks come out of the nozzles and degrades printing quality. As no cooling module is embedded in the printer assembly, it is difficult to stabilize the jetting temperature. This deposition technique is compatible with a wide range of plastic and flexible substrates because of low deposition temperature. The details of Fujifilm printer will be discussed in the next section. As this is a contactless printing, the surface morphology is not an issue during deposition. The pattern formation depends on the surface energy, wettability of the ink, and hydrophilicity of the substrate surface.

The cartridge unit consists of an ink reservoir and a jetting module. The ink is stored in the reservoir fluid bag. The cartridge head has 16 piezoelectric jetting nozzles with a diameter of 21.5 μm each. The nozzles can dispense a droplet of the nominal volume of 10 pL from the cartridge head. The heaters in the jetting module raise the jetting temperature to lower the viscosity for stable ink-jetting. We can adjust the printing head angle with respect to the platen plane using the circular calipers on the printer head.

The angle of the printer head depends on the resolution of the image to be printed. The operation of the printer is controlled by Dimatix drop manager software. The fiducial

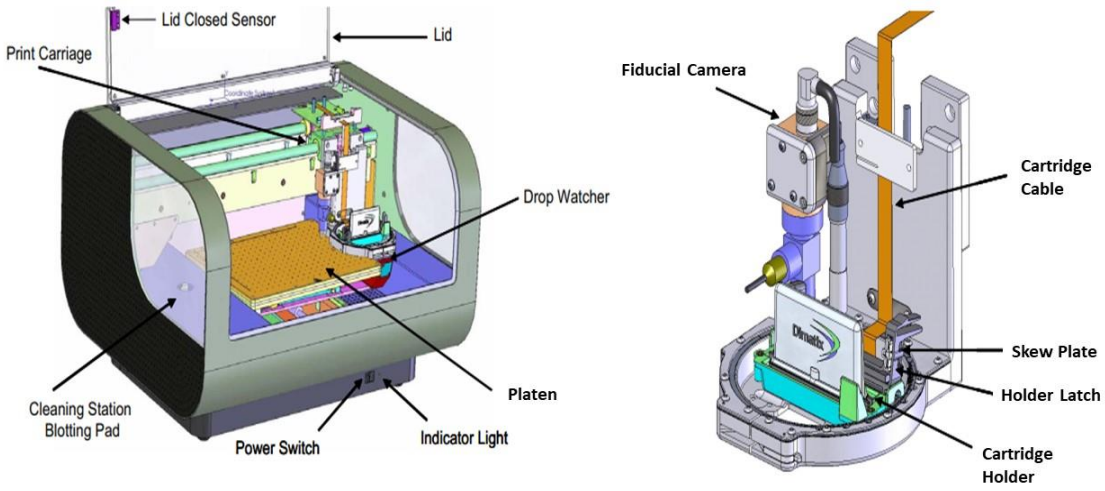

Figure 3. a) Fujifilm Dimatix materials printer, b) Print carriage assembly [13].

camera is used to locate a point on the platen and see the printing conditions. The control software is used to set the print origin, substrate temperature, calculate print offsets, vertical and horizontal distances. The Drop-Watcher allows direct viewing of the jetting nozzles, and the surrounding area around the nozzles. By selecting a specific nozzle, the user can view the jetting of ink through that nozzle. All the sixteen nozzles can jet out ink simultaneously. Each nozzle voltage can be adjusted to control the drop velocity as the voltage is translated into drop velocity through piezoelectric actuation. In the pop-up window, the user can set the cartridge temperature, meniscus setpoint, and cartridge print height. In an inkjet printer, the drop spacing is the center to center distance from one drop to the next in X and Y position. The print head angle depends on the drop spacing value. Higher drop spacing results in a lower density of ink in the deposited area, thus the image

resolution is low. For NDG ink, the optimal drop spacing was determined to be 30 µm. Additionally, to avoid the coffee ring effect, the substrate temperature was set at 60 ^{o}C. The optimum drop spacing for the NDG ink was 30 µm.

1.3.2. Inkjet Printed Semiconductor Devices

Inkjet printed fabrication technology has been explored for applications such as thin film transistors, organic light emitting diodes (OLEDs), solar cells, memory devices, radio frequency tags, RF antennas, and electronic textiles. Inkjet printed organic semiconducting polymers have largely been studied for organic transistors, solar cells, and light emitting diodes as their fabrication processes are much simpler than conventional silicon technology [14]. In this section, we will briefly discuss some of the recently reported inkjet printed electronic devices.

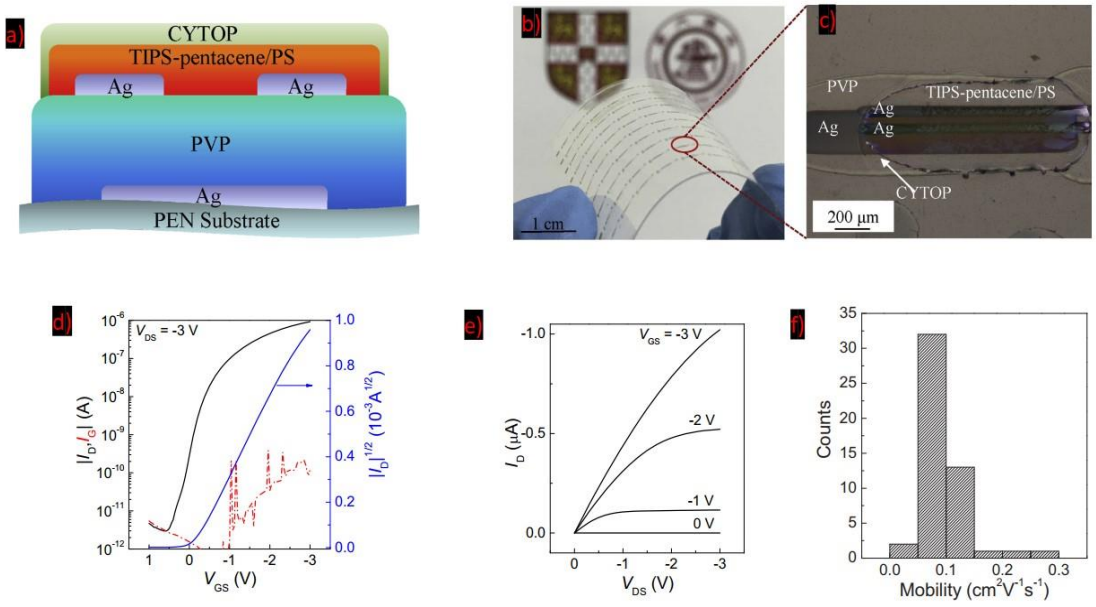

Figure 4. a) Schematic diagram of OTFT, b) Photograph of fabricated flexible sample, c) Polarized optical micrograph of the fabricated device, d) transfer characteristics (I_D-V_{GS}), (e) output characteristics (I_D-V_{DS}), f) Distribution of mobility of 50 OTFTs [15].

Over the last decade, the performance and reliability of inkjet printed organic

transistors (OTFTs) have been improved significantly. Organic transistors and integrated circuit based on OTFTs were demonstrated on plastics, papers, and fabrics. For example, Feng et al. in Ref 15 demonstrated an all inkjet printed OTFT on the flexible substrate. They used poly(4-vinyl phenol) (PVP) for the gate dielectric, 6,13 bis(triisopropylsilylethynyl) - pentacene (TIPS-pentacene)/ polystyrene (PS) blend as the semiconducting layer, and CYTOP for encapsulation layer. Their OFTs showed state-of-the-art performance with a low voltage operation (−3 V), high on/off ratio (3.1×10^5), low threshold voltage (−0.17 V), and a yield rate of 62.5%. Their average device mobility was around 0.1 cm^2/V.s.

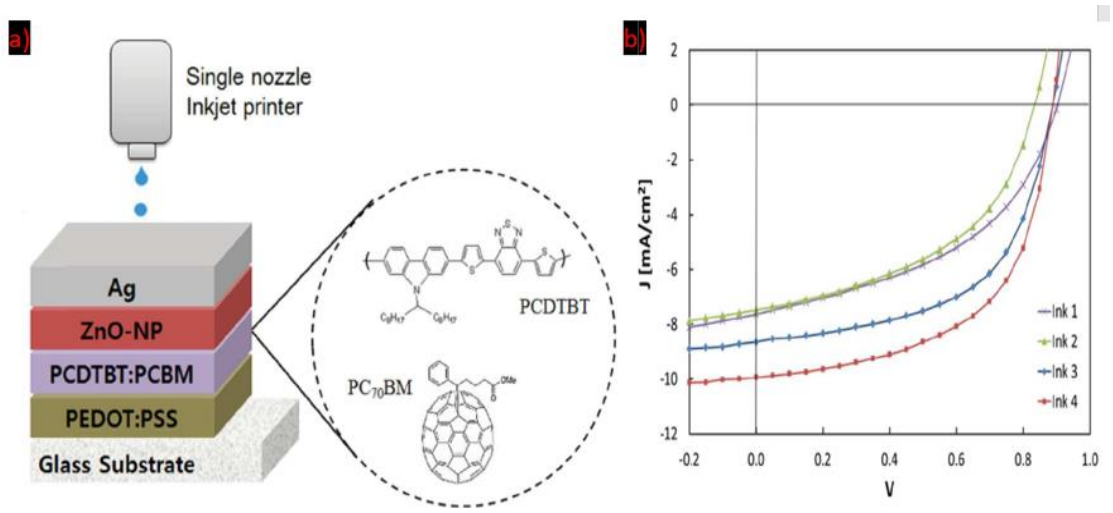

Figure 5. a) Device structure of an inkjet-printed solar cell, b) Summary of device performance with different solvent formulations [16].

A significant effort has been employed to integrate inkjet printed solar cells monolithically along with transistors, sensors, and other components. Sungjune et al. in reference 16 demonstrated an inkjet printed solar cell based on poly(3,4-ethylenedioxythiophene): polystyrene sulfonate (PEDOT:PSS)/poly[N-9′-heptadecanyl-2,7-carbazole-alt-5,5-(4′,7′-di-2-thienyl-2′,1′,3′-benzothiadiazole)]: [6,6]-phenyl-C71-butyric acid methyl ester (PCDTBT: PC 70BM)/ZnO/Ag stacked structure which is

shown in Figure 5a. Their reported solar cell efficiency of 5.05% is the maximum efficiency for the inkjet printed solar cells to date. Additionally, inkjet printed flexible resistive memory, passive UHF RFID, and OLEDs were reported in literature [17, 18, 19].

1.4. Thesis Overview

This thesis is divided in a total five chapters. The current chapter covers an introduction and a summary of the research, background of inkjet printing, a brief description of Fujifilm Dimatix Printer, and the printed semiconductor devices. Chapter II focuses on the basic properties of graphene, doped graphene, and molybdenum disulfide materials. Finally, Chapter II ends with an extensive literature review of inkjet printed 2D material transistors and the motivation and goals of my thesis. Chapter III investigates the ink preparation, and thin film characterization of the liquid exfoliated materials. The inks and thin films were characterized by UV-vis spectroscopy, the surface profiler, scanning electron microscopy, and Raman spectroscopy. Chapter IV discusses the design, fabrication, and characterization of all inkjet printed NDG and NDG/MoS_2 heterojunction field effect transistor. Additionally, the transistor test results are compared with state-of-the-art reports. Finally, a summary, conclusion, and suggestions for future works are given in Chapter V.

II. LITERATURE REVIEW

2.1. Graphene

Since the discovery of two-dimensional materials, they have been in the center of research for more than a decade because of their exciting and unusual properties. Graphene is the front-runner in this race due to its one atomic layer thickness, high carrier mobility, extreme mechanical strength, and optical transparency [19]. Graphene has many attractive properties such as high transparency (97.7% transmittance), high thermal conductivity (3×10^3 W/m K), high mobility of charge carriers (~200,000 $cm^2V^{-1}s^{-1}$), and high Young's modulus (1.1 TPa) [20]. Graphene has honeycomb two-dimensional lattice structure as shown in figure 6a. It is a zero-band gap semimetal in which the valence and conduction bands are cone-shaped, and they meet at the K-point of the Brillouin zone.

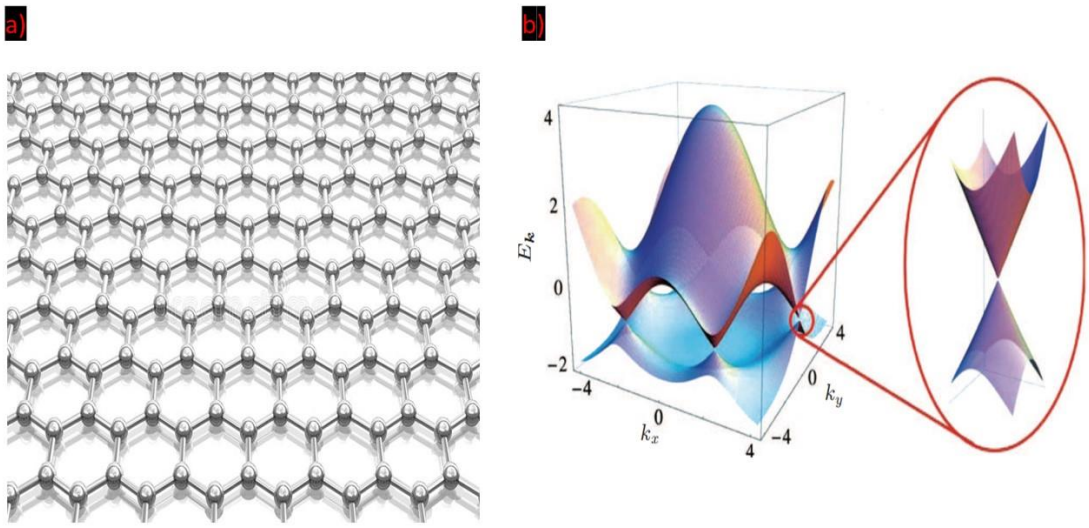

Figure 6. a) Honeycomb lattice structure of graphene, b) Band structure of pristine graphene with zero band-gap.

Due to the absence of band-gap, the typical current on/off ratio of graphene-based TFTs were around 5. Researchers from IBM demonstrated a large area graphene transistor with

a current on/off ratio of 100 at room temperature [21]. Just like regular thin film graphene TFTs, inkjet printed graphene transistors showed on/off ratio of around 10 [8]. The absence of band-gap in graphene hinders its application in switching circuits. Due to zero band-gap, it is difficult to turn graphene TFTs off. For switching applications, a current on/off ratio between 10^4 to 10^7 and a band-gap larger than 0.36 eV is desirable [22].

2.2. Band-Gap Opening in Graphene

The band-gap is crucial for switching operation of transistors with graphene channel. Several attempts have been taken to open the band-gap in graphene through graphene–substrate interaction, chemical substitution doping, and quantum confinement. Melinda et al. in reference 23 demonstrated a band-gap opening of 0.2 eV in graphene nanoribbon (width ~ 15 nm). The lateral confinement of charge carriers in graphene was created by lithographically patterned metal electrodes. Zhou et al. in reference 24 showed a band-gap opening of 0.26 eV in epitaxial graphene on silicon carbide (SiC) substrate. This gap was originated from the breaking of sublattice symmetry from graphene-substrate interaction [24]. The angle resolved photoemission spectroscopy (ARPES) intensity map is shown in figure 7a for single-layer graphene on the 6H-SiC substrate. The band-gap decreased as the number of layers increased and disappeared when the number of layers exceeded four. In bilayer graphene, a tunable band-gap of maximum 0.22 eV was reported by applying vertical electric field [25]. Several groups reported band-gap opening in graphene using chemical doping. The band-gap opening in graphene using various mechanism is summarized in Table -1. Warmuth et al. reported band-gap opening of 0.42 eV in single layer graphene due to the bismuth (Bi) intercalation on Ir(111) substrate as shown in figure 7b [26]. The Density Functional Theory (DFT)

analysis of nitrogen doping in monolayer, bilayer and few-layer graphene predicted the band-gap opening in nitrogen-doped graphene [27]. Several methods have been developed to dope graphene with nitrogen, such as ammonia precursor flow during chemical vapor deposition (CVD) growth of graphene, arc discharge, embedded nitrogen and carbon within the metal substrate, ion implantation and ammonia or nitrogen plasma treatment and a band-gap of 0.25 eV was achieved [28]. Besides nitrogen, it is possible to

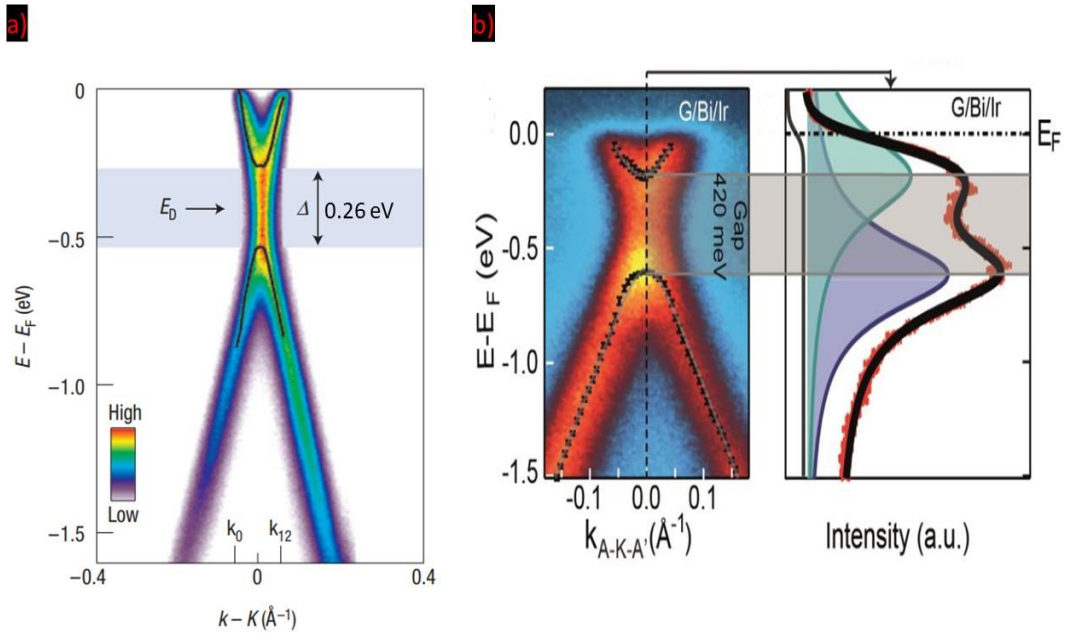

Figure 7. a) ARPES intensity maps taken on single-layer graphene on 6H-SiC [24], b) Band-gap opening in graphene with bismuth intercalation on Ir (111) surface [26].

open band-gap in graphene using triazine, twisted sodium nanostrips, boron nitride doping [29-31]. Because of the band-gap opening in NDG, it has a great potential to be an excellent material for inkjet printed transistors with high current on/off ratios provided that the NDG nanosheets are available from vendors like Sigma-Aldrich, ACS materials. It is also possible to break the 1-5 layer nanosheets to 1-2 layer nanosheets through dry sonication.

Table 1. Band-gap opening in graphene.				
Process	Dopant	Graphene Synthesis	Band-gap (eV)	Reference
Graphene nanoribbon	N/A	Micromechanical cleavage	0.2	[23]
Electrostatic doping	N/A	Micromechanical cleavage	0.22	[25]
Substrate-graphene interaction	N/A	Thermal decomposition of SiC	0.26	[24]
Chemical doping	Bismuth	Chemical vapor deposition	0.42	[26]
Chemical doping	Nitrogen	Chemical vapor deposition	0.25	[28]
Chemical doping	Triazine	Mechanical exfoliation	0.11	[29]

2.3. Molybdenum Disulfide

To overcome the limitation of graphene, researchers have been exploring other two-dimensional (2D) materials. Molybdenum disulfide (MoS_2) is one of the most studied 2D materials after graphene. It is a layered transition metal dichalcogenide (TMD) with a sandwich structure of three hexagonal atomic layers, namely sulfur-molybdenum-sulfur structure. Atoms are connected to each other by strong covalent bonding which forms two dimensional (2D) layers, and the layers are bound with each other via weak van der Waals interaction [32]. Mono and few-layered MoS_2 have a direct bandgap of 1.9 eV, while bulk MoS_2 has an indirect bandgap of 1.29 eV. The extensive research on 2D TMDs was spurred by the first reported high mobility (> 200 $cm^2 V^{-1} s^{-1}$) single layer MoS_2 transistor [33]. Following the success of high mobility transistor, high performance electronic devices such as photodetectors, sensors, flash memory based on

TMDs have been reported. Majority of those MoS_2 devices were built from MoS_2 flakes produced by mechanical exfoliation of bulk MoS_2. Mechanical exfoliation is not a suitable method for large area devices due to limited flakes size. Inkjet printing of MoS_2 has a high potential for fabricating large area devices.

2.4. Inkjet-Printed 2D Materials Transistors

A field effect transistor (FET) is a transistor that uses an electric field to control the current flow along the channel and can be used as a switch and an amplifier. A FET device allows the free propagation of an electrical signal from the input to output and performs DC switching. For switching purposes, transistors have relative advantages compared to mechanical switches. They are small, have no moving parts, operate with voltage, and current, and perform fast switching. They can be used as an integral part of a circuit or independent components of a system to perform amplification and switching operation. All inkjet printed transistors are expected to perform both switching and RF operation.

Currently, a large variety of inks based on organic semiconducting polymers, carbon nanotube, graphene, and molybdenum disulfide are available to make thin film transistors (TFT). They suffer either from very low mobility or low current on/off ratio. It is crucial to explore new material inks compatible with current inkjet printing technology and their TFTs with high mobility and high current on/off ratio. We will utilize the possible ways to improve the current on/off ratio in the 2D material-based inkjet printed transistor along a with reduced number of fabrication steps.

Inkjet-printed (IJP) and liquid phase exfoliated (LPE) graphene and MoS_2 materials were synthesized by several groups before. However, current on/off ratios for

those transistors were very low. In fact, liquid phase exfoliated MoS_2 exhibited Schottky barriers with source-MoS_2 and drain-MoS_2 terminals [34]. Now, a brief discussion on inkjet printed graphene transistors, liquid exfoliated, and inkjet printed MoS_2 transistors will be covered in this section.

Torrisi et al. reported an inkjet printed bottom-gate graphene transistor on Si/SiO_2 [8]. Their reported on/off ratio and mobility were 10 and 95 $cm^2/V.s.$ respectively. The current-voltage measurements were performed at room temperature. However, the reported transistor was not all inkjet printed and required HMDS (Hexamethyldisilazane) treatment to improve the adhesion to the substrate. The transistor had well-defined charge neutrality point and p-type device behavior. The transistor required higher V_{ds} and V_{gs} for saturation which is not suitable for device applications.

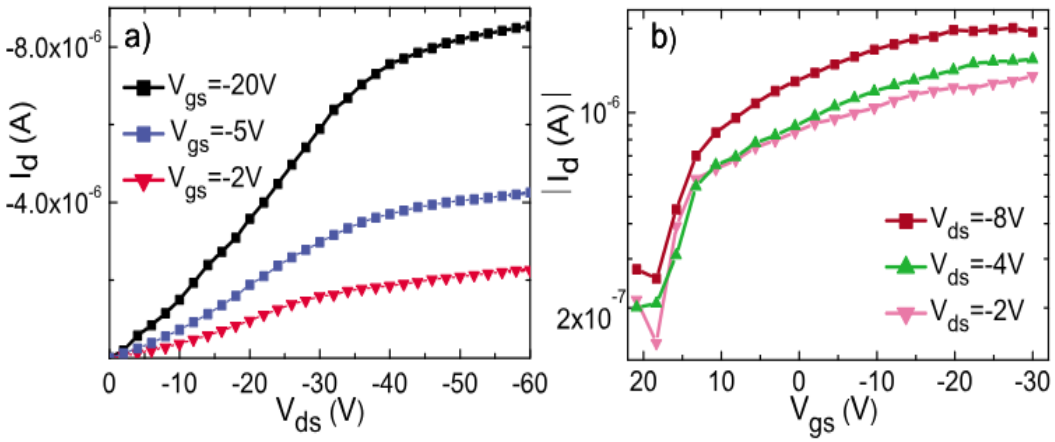

Figure 8. a) Output and b) transfer characteristics of an inkjet printed graphene TFT [8].

Li et al. demonstrated an inkjet printed graphene transistor on Si/SiO_2 with printed silver source and drain electrodes [10]. The Dirac point which is a signature of graphene transistor, was absent in their report. With an increase in the number of printed layers, the drain currents did not modulate significantly as shown in Figure 9a. The current on/off

ratio was about 1.25 and device mobility was 0.12 cm^2/V.s. respectively. The I_d-V_d curves did not saturate for a wide range of gate voltage as shown in Figure 9b. These printed transistors are not the best graphene TFTs for actual application.

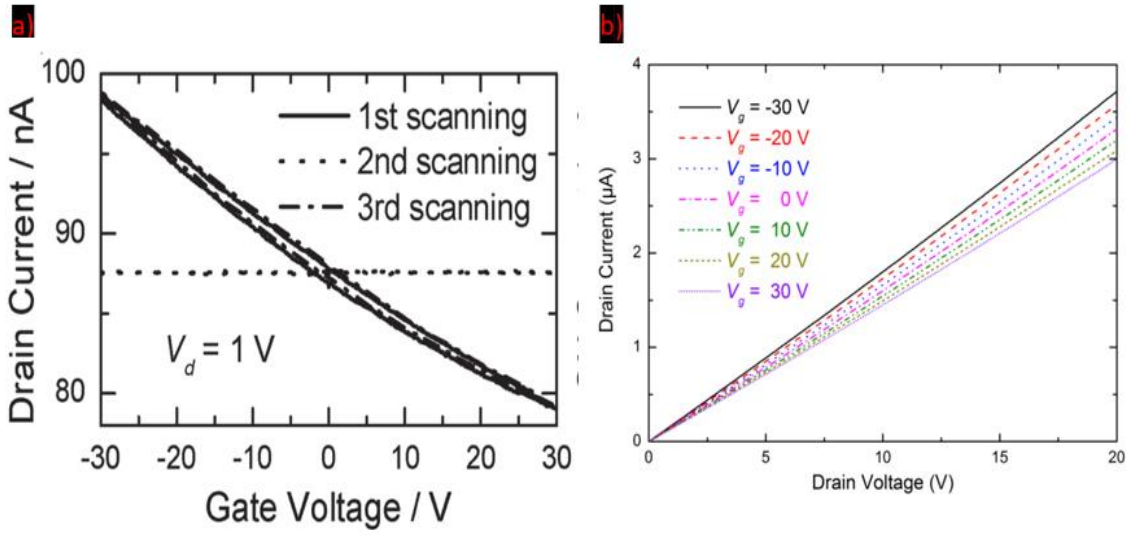

Figure 9. a) Transfer characteristics of a six-layer TFT with channel length about 480 μm, b) Output characteristics of a six-layer TFT with channel length about 240 μm [10].

Recently, all inkjet-printed graphene transistors were reported for wearable and textile electronics [35]. The graphene TFTs displayed well-defined Dirac points for both bottom-gate coplanar and inverted-staggered transistor structures on fabrics. The TFTs were operating at low voltages and had high mobility. However, the current on/off ratios were still small (about 2.5).

Inkjet-printed MoS_2 transistors have been prepared by dispersing bulk MoS_2 powder into appropriate solvents via liquid phase exfoliation. Researchers investigated MoS_2 transistors with both liquid exfoliated MoS_2 and inkjet printed MoS_2. Coleman et al. first reported the synthesis of TMD materials via liquid phase exfoliation [36]. An SEM image of liquid phase exfoliated MoS_2 and a transistor based on it, are shown in Figure 10a-b. The output and transfer characteristics of the liquid exfoliated MoS_2

transistor are depicted in Figure 10c-d. The active channel length of the transistor was less than 1 µm. Individual flakes showed small on-off ratios (<10) with the mobility between 0.01 and 0.02 cm^2/Vs. Likewise, the non-linear, and symmetric I_d-V_d characteristics were reported earlier for liquid exfoliated MoS_2 [34]. This symmetric behavior was attributed to the formation of Schottky barriers between drain-MoS_2 and

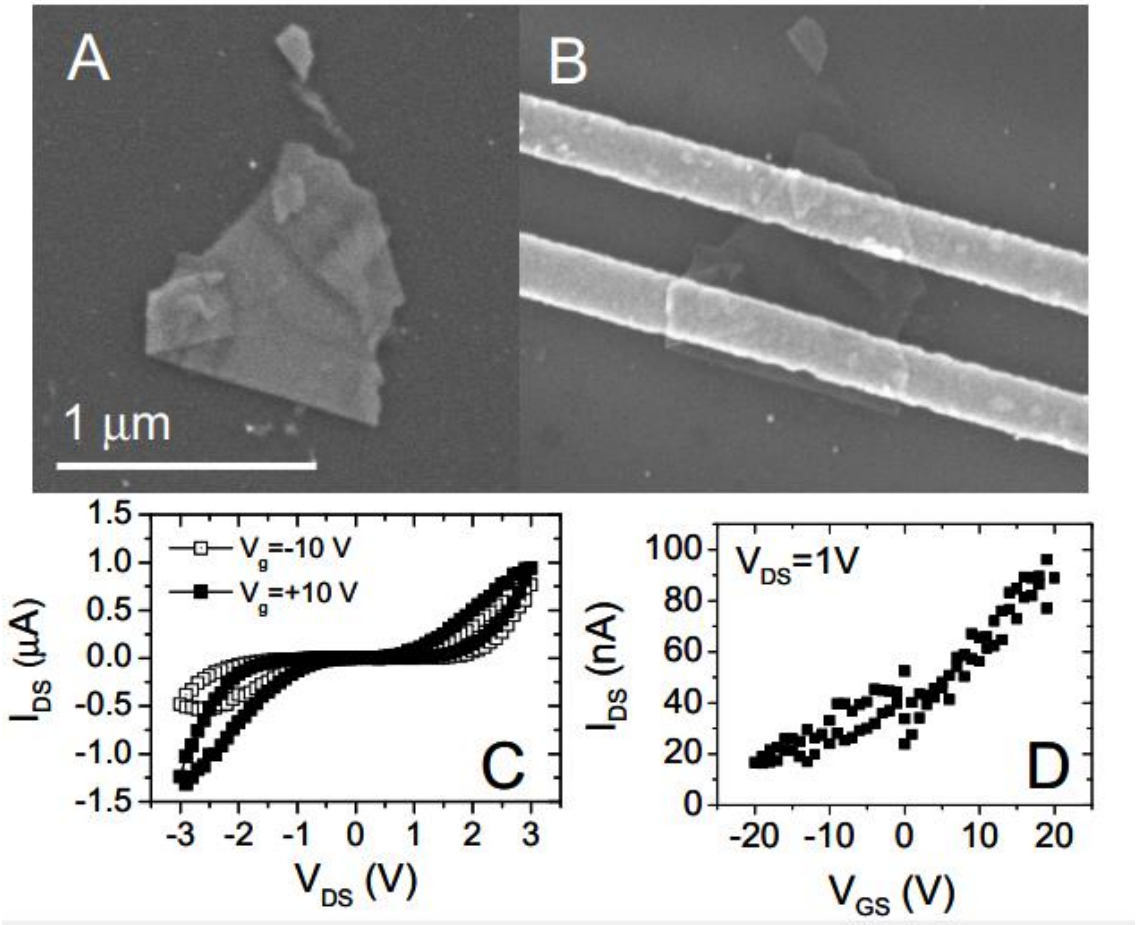

Figure 10. A) An SEM image of an MoS_2 flake in Si/SiO_2. B) the same flake after Cr/Au electrode deposition. C) Source-drain current voltage characteristics. For gate voltages of +10 V and –10 V. D) Gate voltage dependence for a source-drain voltage of 1V [36].

and source-MoS_2 terminals [34]. The transistors reported in reference 34 had current on/off ratios between 3 to 4 with device mobility of 0.117 cm^2/Vs. The devices were fabricated on Si/SiO_2 with predefined interdigitated electrodes (IDEs) of channel length

1µm. The long channel and large area solution-processed MoS_2 TFTs were reported by Qiyuan et al. in reference 37. Flexible MoS_2 TFT arrays were fabricated for gas-sensing applications. The reported on/off ratio was ~ 10. To our best knowledge, no liquid exfoliated MoS_2 had current on/off ratio higher than 10. Inkjet printed MoS_2 transistors were fabricated by Östling's group on Si/SiO_2 using printed silver drain and source electrodes [32]. The gate modulation (I_d - V_{gs} characteristics) curves were unusual compared to other inkjet printed transistors as shown in Figure 11a. The drain current change was very small which is obvious from the output characteristics (Figure 11b). The reported on/off ratio was very small (~2).

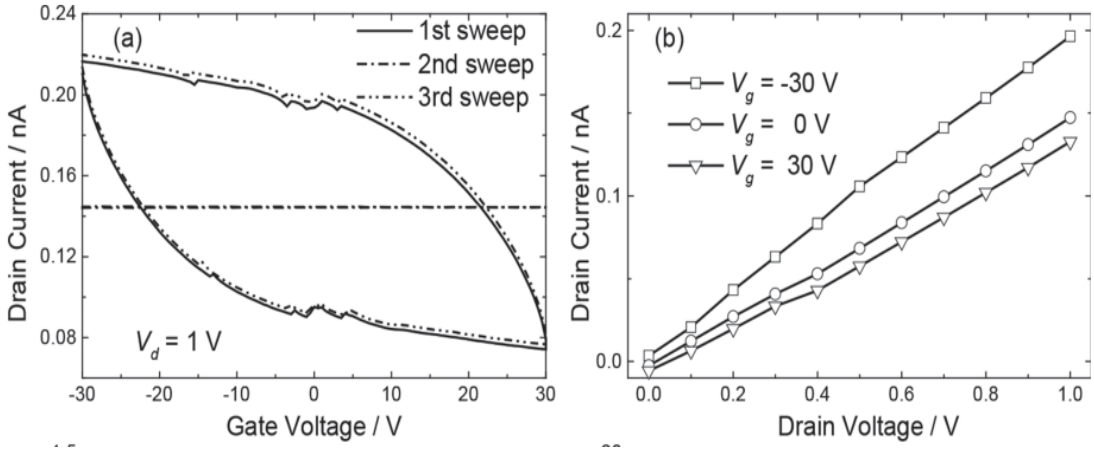

Figure 11. a) Transfer characteristics for a printed MoS_2 TFT (L = 13 µm), b) output characteristics for the same device [32].

Based on our literature review, it is evident that the inkjet printed transistors with two major 2D materials are suffering from the low current on/off ratios, regardless of the device mobility. Currently, there are a few 2D materials available to work with. There is no all inkjet-printed MoS_2 device reported to date. The devices available in the literature are mostly bottom-gated device which is not suitable for practical application. Inkjet printed TFTs have low current on-off ratios, and, they have a lot of reliability issues

which are yet to be resolved. For the development of high on-off ratio inkjet printed transistors, it is indispensable to search for new materials, try all the possible ways to improve the current ratio and find suitable application areas for them. This is the problem addressed in this proposed research.

III. INK AND THIN FILM CHARACTERIZATION

3.1. Introduction

The progress of printed electronics is crucial for developing flexible devices, with immense research focusing on developing new materials [38]. All inkjet printed circuits consisting of electronic devices, interconnects, and RF devices based on material nanosheets are an important goal in nanoscience. Graphene and other 2D material inks have enabled many inkjet-printed devices, including TFTs, photodetectors, sensors, supercapacitors, and solar cells. Single or multilayer 2D material inks can be developed by exfoliating material nanosheets into the solution via liquid phase exfoliation (LPE). Nanosheets of 2D material inks can be deposited with different printing techniques such as inkjet, spray, flexographic, screen, and gravure printing. The materials can be arranged into heterostructures, which create a materials assembly with novel properties which are different from the original one. In this research, a novel ink with NDG nanosheets and its transistors were investigated. Finally, NDG and MoS_2 were arranged into a heterostructure to create novel properties which are different from individual NDG and MoS_2 nanosheets.

3.2. Ink Preparation

Nitrogen-doped graphene (NDG) powder was purchased from Sigma-Aldrich (product no. 900527). NDG powders were composed of NDG nanosheets with a typical thickness of 1 to 5 layers, lateral size of 0.5 to 5 μm, and nitrogen content of 2 to 4%. NDG nanosheets were dry-sonicated for 10 hours to break the thick flakes because the lateral size of the flakes should be at least 1/50 of the nozzle diameter (a ~ 21.5 μm) to prevent the nozzle clogging. An SEM image of NDG flakes is shown in Figure 12, after

dry sonication. The NDG nanosheets are composed of many thin NDG wrinkles. The lateral size of the NDG nanosheets are less than 1 μm. It is obvious from the randomly protruding nanosheets that they are composed of many single layer NDG. The NDG nanosheets stick together to form this crumpling structure.

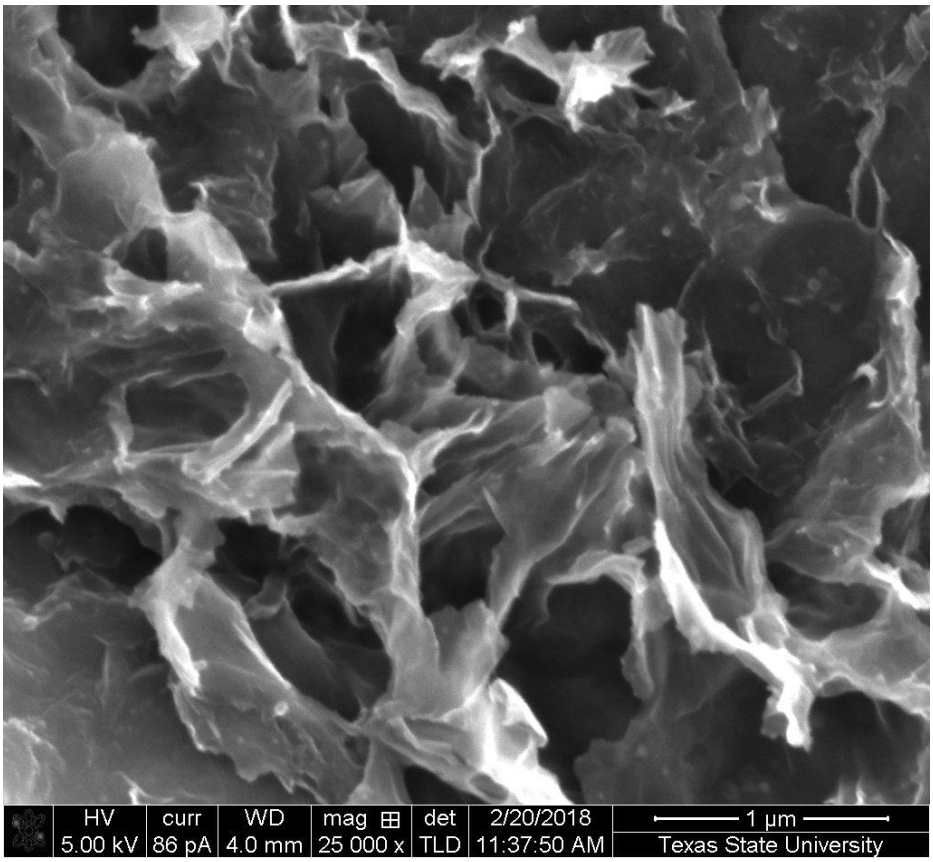

Figure 12. SEM image of NDG flakes after dry sonication.

Raman is one of the most common vibrational spectroscopies for fingerprinting carbon species, including three-dimensional (3D) graphite and diamond, 2D graphene, one-dimensional (1D) carbon nanotubes, and zero-dimensional (0D) fullerenes. The Raman spectrum of NDG nanosheets on Si/SiO_2 substrate was obtained with the Horiba LabRAM HR evolution Raman spectrometer. The laser excitation of 532 nm was used at 100× objective, with an incident power less than 1 mW to avoid sample damage. Figure

13 shows the Raman spectrum of NDG powder after dry-sonication. The NDG shows two intense peaks which are D (~ 1341 cm^{-1}) and G (~ 1578 cm^{-1}) bands respectively. Moreover, there are two additional peaks 2D (~ 2670 cm^{-1}) and D + D' (~ 2904 cm^{-1}) bands respectively. The G and 2D peaks are the signature of graphene-like structure in nanosheets. The G band corresponds to E_{2g} phonons at the Brillouin zone center. The G-band arises from the stretching of C-C bonds in a sp^2 hybridized carbon system. The D-band is related to defects in sp^2 hybridized carbon materials, which is activated by an inter-valley double resonance (DR) Raman process. The intensity ratio I_D / I_G of 1.005 indicates a high degree of disorder due to nitrogen doping. The strong D peak can also originate from the submicrometer flakes boundaries, and vacancies. The 2D peak is the secondary D peak, which appears at around 2700 cm^{-1}. For single layer graphene, the 2D band shows sharp-peak and high intensity compared to D and G peaks [39]. The 2D band broadens and intensity reduces with the number of graphene layers. If the number of graphene layers exceeds five, the 2D band becomes like bulk graphite. In the Raman spectrum of Figure 13, the intensity of the 2D band is much smaller compared to the D and G bands. Given that the NDG nanosheets are of 1-5 layers in the manufacturer technical datasheet (TDS), and sonication converts many of nanosheets into a single layer, we attribute the low intensity of the 2D band to doping and lattice defects [40]. The intensity of the 2D peak is strongly dependent on the electron/hole scattering rate [41]. As nitrogen dopants create defects as well as doping, both effects would increase the scattering rate, which in turn reduces the intensity of the 2D peak. This Raman spectrum strongly agrees with the Raman spectra previously report for NDG synthesized by chemical vapor deposition at 800 and 900 ^oC [42].

The NDG ink was prepared by dispersing NDG flakes into terpineol/cyclohexanone. The NDG powder (~ 5 mg, Sigma-Aldrich product no. 900527) was dry-sonicated for 10 hours to break the bigger particles. For a 10 mL solution, 1.5 mL of terpineol was used as the key solvent. To curtail the viscosity of terpineol, 8.5 mL of cyclohexanone was added. Then, ethyl cellulose of 48 mg was mixed into the solution and sonicated for 1 hour. Finally, the dry-sonicated NDG powder (~ 5 mg) was poured into the solution. The resulting suspension was sonicated for 20 hours, and then centrifuged at 5000 rpm for 30 minutes to remove the thicker flakes. After centrifugation, the suspension was left to settle overnight. The final ink was filtered out from the residue and ready for characterization.

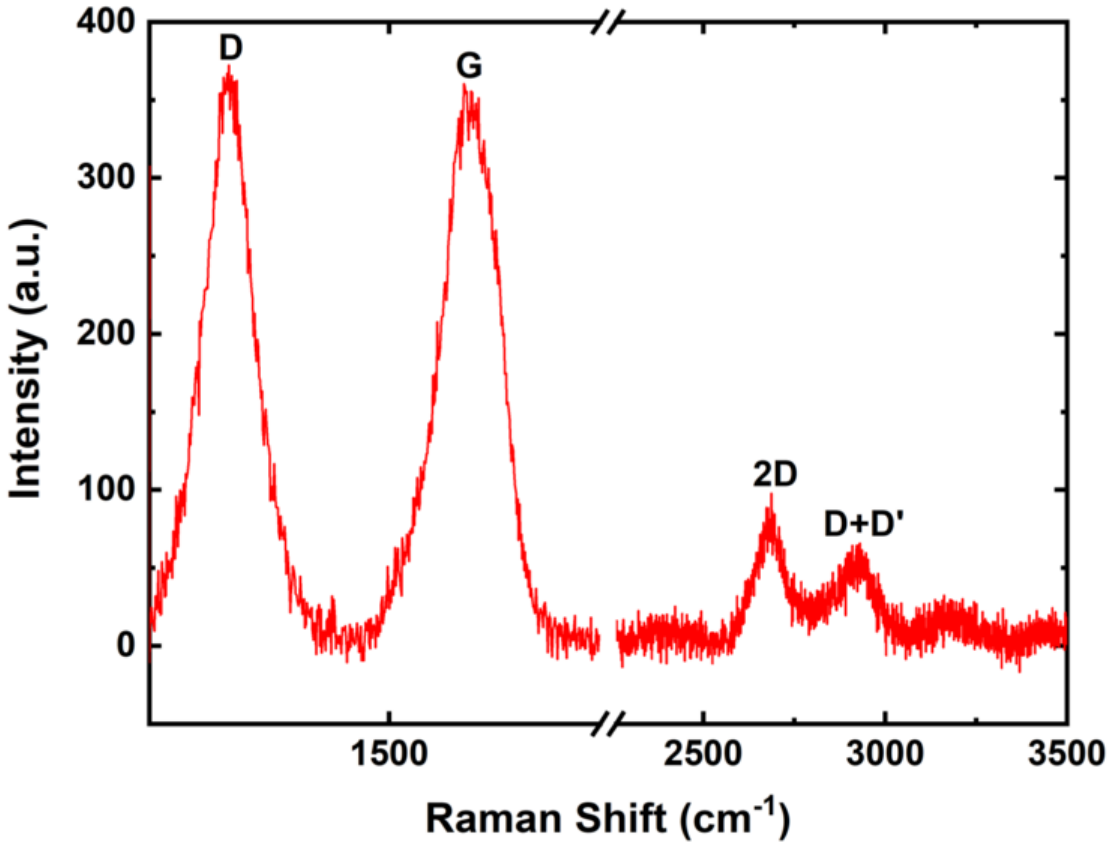

Figure 13. Raman spectrum of NDG nanosheets.

3.3. NDG Ink Characterization

For a drop-on-demand (DOD) inkjet printing, the material inks must have the ability to generate droplets. The droplets ejecting out from a nozzle are influenced by ink viscosity η (mPa s), surface tension γ (mN/m), particle density ρ (gcm^{-3}), and nozzle diameter a (μm). For inkjet printing of an ink, the inverse Ohnesorge number ($Z = Oh^{-1}$) is used as the figure of merit (FOM) to characterize the drop formation and jettability of an ink. Z is calculated by using $Z = (\gamma \rho a)^{1/2} / \eta$ and an optimal range of Z between 1 to 14 is required for stable DOD printing [8].

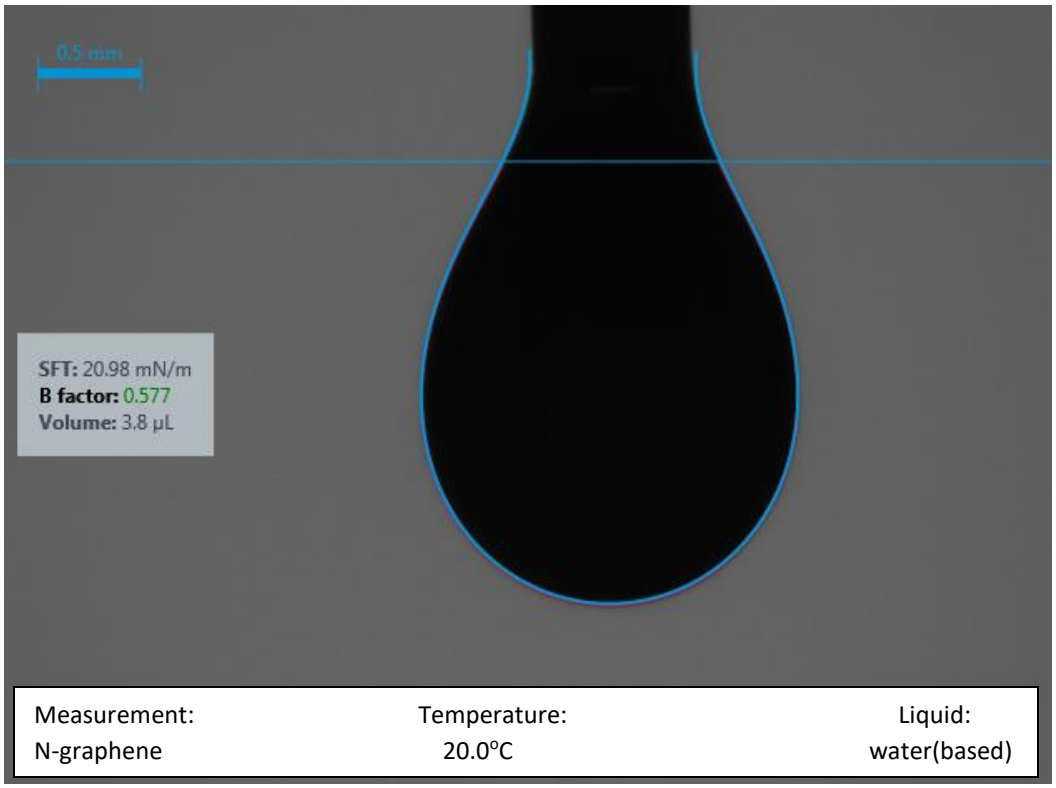

Figure 14. Surface tension measurement of ink.

The surface tension of NDG ink was measured using the pendant drop method (First Ten Angstroms FTA10000B). A small amount of ink (3.8 μL) was suspended from a needle and surface tension was extracted from the software image as shown in Figure

14. The ink density is $\rho = m/V$, m is the mass of ink in grams and V is volume of ink in mL. The ink density ρ for NDG ink was 1.054 g cm^{-3}. The viscosity of the ink was measured with the RheoSense m-VROC viscometer. The viscosity of NDG ink was approximately 2.94 mPa s. For NDG ink, using η = 2.94 mPa.s, γ = 20.98 mN / m, ρ = 1.054 g cm^{-3}, a = 22 μm, we obtain $Z = (\gamma \rho a)^{1/2} / \eta \simeq 7.50$, which is within the conventional range for inkjet printing. There were no satellite drops following the primary drops which was confirmed by capturing the dynamics of drop formation.

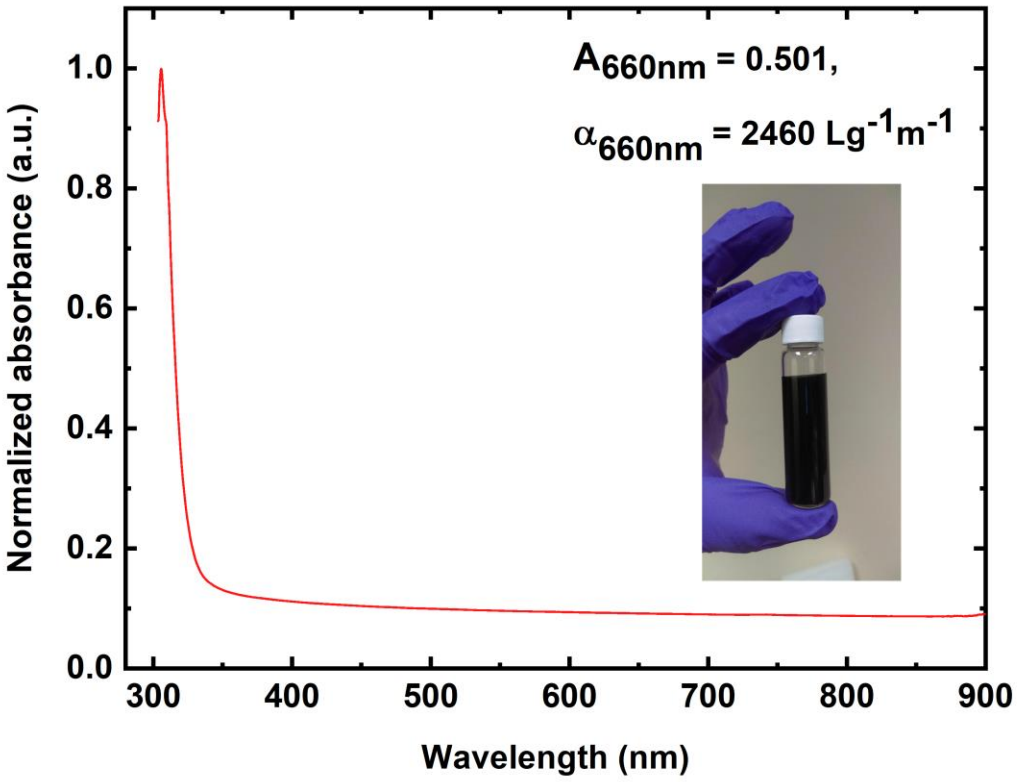

Figure 15. Optical absorption of the N-graphene ink shown in the inset.

The concentration of nanosheets can be calculated from the UV-vis absorbance spectrum via the Beer-Lambert law. The Beer-Lambert law can be expressed as A = αcl, where A is the absorbance, α is the absorption coefficient ($Lg^{-1}m^{-1}$), c is the concentration of dispersed graphene (g/L), and l is the light path length (m). The optical absorption of

the NDG ink is shown in Figure 15, which was diluted to isopropyl alcohol (IPA) at a ratio of 1:20. The spectrum is mostly featureless due to the linear dispersion of the Dirac electrons, whereas the peak in the UV region is a signature of Hove singularity in the graphene density of states [35]. From A = 0.501, $\alpha = 2460\ Lg^{-1}m^{-1}$, l = 0.01 m, our estimated NDG concentration is 0.4 mg/mL [43].

3.4. Thin Film Characterization

Thickness profile is important to predict the behavior of the inkjet printing. Several rectangular patterns were printed on SiO_2/Si using Fujifilm Dimatix materials printer (DMP 2800) and annealed at 375 ^oC. The thickness was measured for a 0.5×0.5 cm^2 sample with different printing repetitions using KLA Tencor p7 surface profiler. The thickness increases linearly as a function of printing passes as depicted in Figure 16. With five printing passes, the thickness was comparatively lower as the nanosheets were assembled to form percolation clusters on the substrate from the scratch.

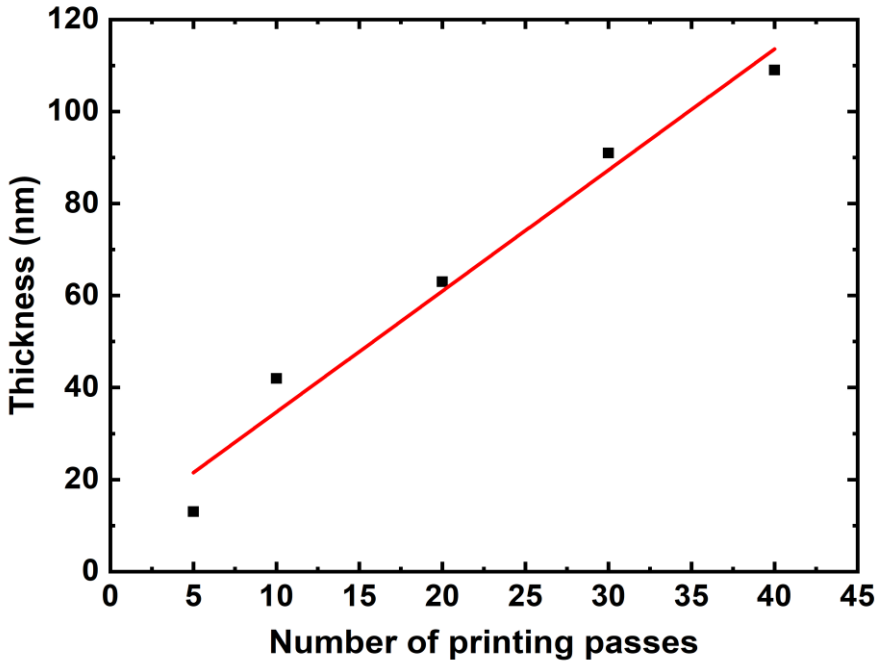

Figure 16. Thickness as a function of printing passes.

Uniformly distributed networks of nanosheets are essential for TFT device performance. Earlier the percolation threshold of 25 nm was reported for the graphene flakes forming a graphene film on an HMDS treated Si/SiO_2 substrate [8]. However, top-gated TFTs require thicker film compared to the percolation threshold to ensure full coverage of nanosheets over the defined area. For example, Carey et al. in reference 7, printed 100 nm thick graphene films for all top-gated TFTs. Hence, we conducted a study on surface morphology change with the number of printing passes. Figure 17a shows the corner of a printed pattern. The ink distribution was quite uniform over the defined area.

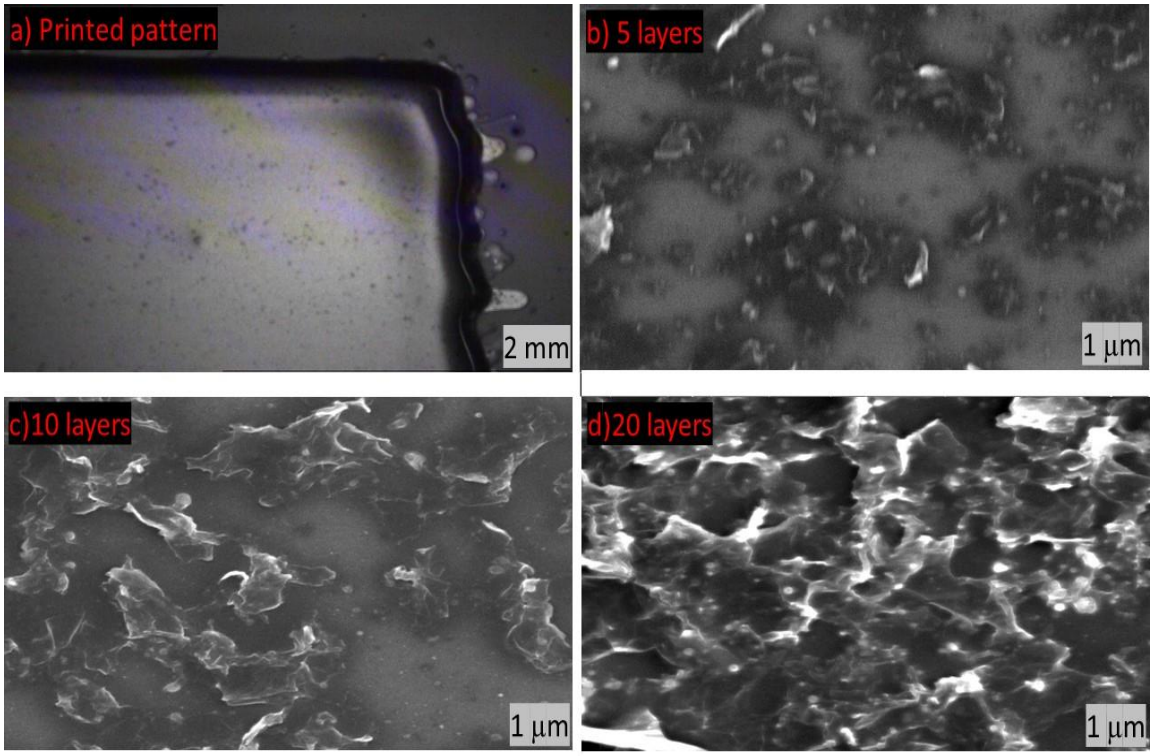

Figure 17. a) Corner of a printed N-graphene pattern, SEM image of N-graphene films of b) 5 layers, c) 10 layers, and 20 layers.

Figures 17b-d show the SEM images of printed NDG for 5, 10, and 20 layers respectively. The top surface area coverage of NDG flakes is quite low for 5 printing passes with small flakes randomly distributed over the area. This corroborates the claim

of breaking the nanosheets to a few hundred nanometer lateral size flakes. In 10 printed layers, the lateral size of flake's percolation network increases as more nanosheets agglomerate with the number of layers. For 20 layers, it is composed of many NDG wrinkles and most of the area is uniformly covered by the nanosheets. The flakes' lateral dimensions are less than 1 µm.

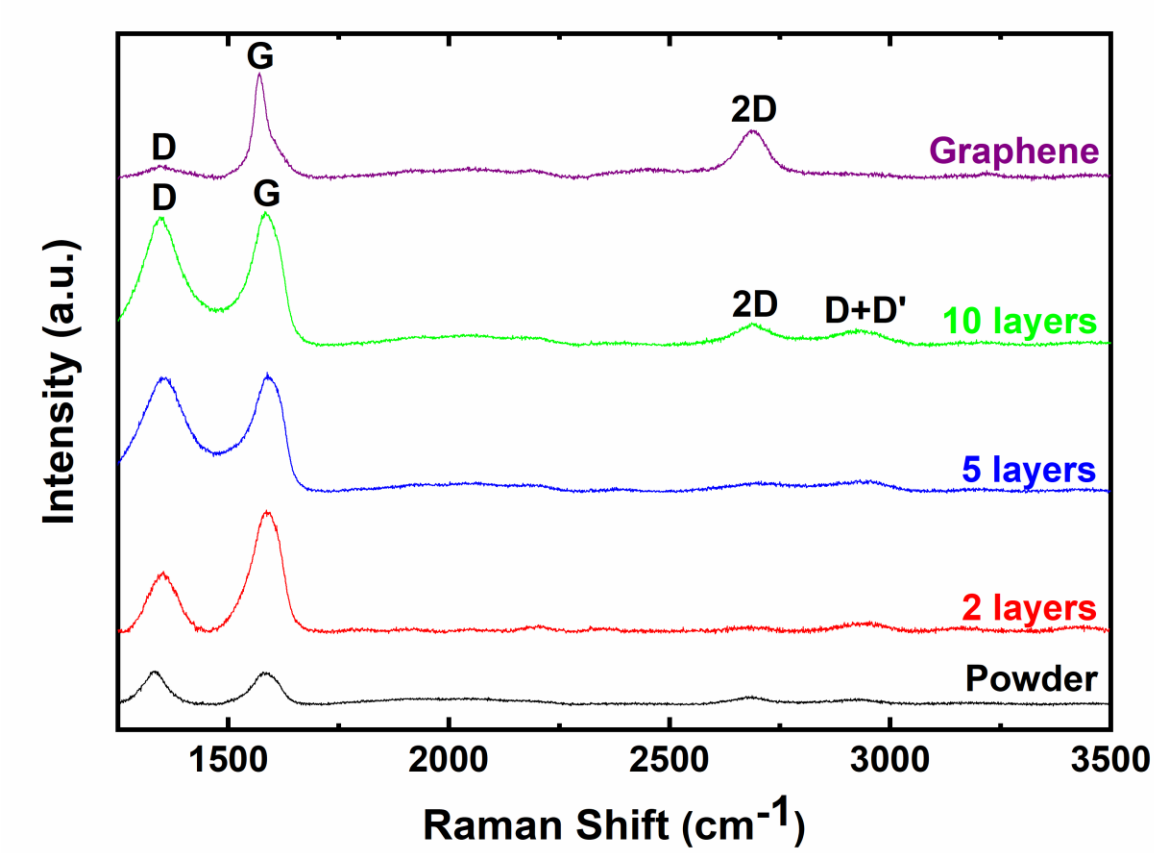

Figure 18. Raman spectra of NDG flakes,2,5, and 10 layers compared with Raman spectrum of graphene.

Figure 18 compares the Raman spectrum of inkjet printed graphene film with the Raman spectra of NDG powder, and printed layers. Just like NDG powder, the Raman spectra of the printed thin films have D, G, 2D, and D+D' peaks respectively. The peaks of the Raman spectra remain almost constant with additional printing passes. The distribution of Raman bands of printing layers remains alike to the NDG powder. The

I_D/I_G ratio for 2 layers is small compared to the I_D/I_G ratios of NDG flakes, and printed layers (5, and 10). This also suggests inhomogeneous defects in the nanosheets. As the I_D/I_G ratios for printed layers are mostly less than the I_D/I_G ratios of the NDG powder (Figure 19a), the solvent-induced contaminations/defects in NDG films are negligible. We compared the Raman spectra of NDG to the Raman spectrum of graphene which was reported before [44]. As compared to NDG, the G band is steeper in graphene. The intensity of 2D bands in NDG is still lower despite the flakes being few-layer graphene (FLG). The defects in printed graphene are much lower than NDG nanosheets. There is no D+D' band in the Raman spectrum of graphene.

The I_D/I_G ratios are plotted in Figure 19a for different printing passes. The I_D/I_G points are randomly distributed for different printing repetitions. The I_D/I_G ratios alter over a wide range from 0.256 to 0.979. This indicates that the distribution of the dopants in nanosheets are inhomogeneous. The I_D/I_G ratios for 2 layers are lower relative to 5 and 10 layers. Figure 19b presents the relation between the I_{2D}/I_G ratios to the doping concentration (I_D/I_G). The I_{2D}/I_G ratio has no definite relation Therefore, I_{2D}/I_G cannot be used to quantify the doping concentration and the number of layers. Figures 19c-d describe I_D/I_G ratios as a function of G and 2D band peak positions. We observed strong blueshifts (the shifting of peaks toward higher wavenumbers) in G and 2D peaks in the printed layers. The highest amount of blueshifts in printed layers are ~25 cm^{-1} and 31 cm^{-1} for G and 2D peaks with respect to NDG flakes. The blueshifts in the Raman spectra are caused by doping and strain. In the preceding section, we argued that the solvent-induced doping in nanosheets is negligible. Therefore, we ascribe these blueshifts to compressive/tensile strains in NDG nanosheets in printed thin films [40]. These strains

are induced by the random distribution of printed flakes rather than the lattice mismatch.

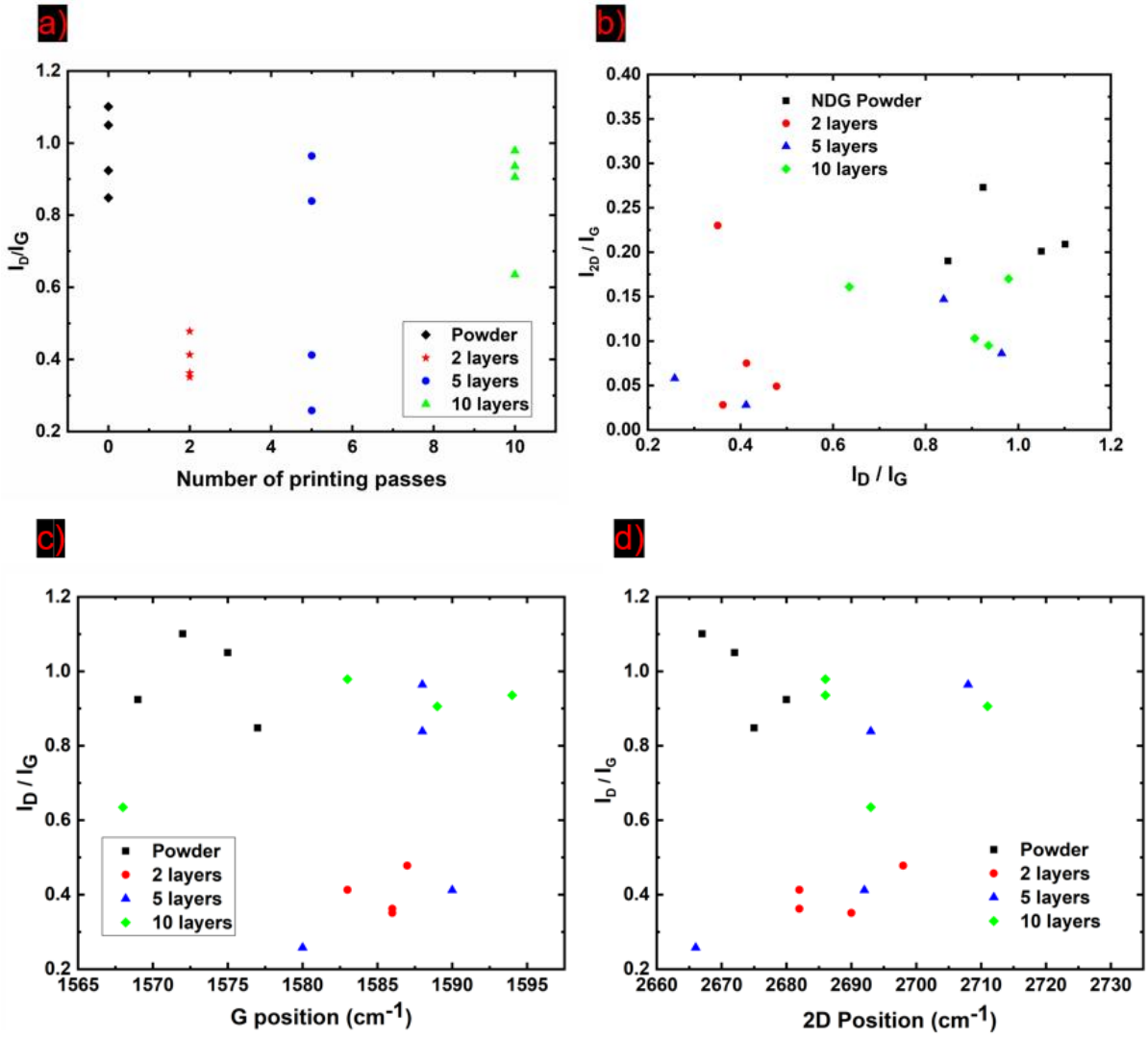

Figure 19. a) Distribution of I_D/I_G ratios with number of printing passes, b) Distribution of I_{2D}/I_G ratios with doping concentration, I_D/I_G ratios as a function of c) G-peak position, and d) 2D-peak position.

3.5. MoS_2 Ink Preparation and Characterization

The MoS_2 ultrafine powder was purchased from Graphene Supermarket. The key solvent, NMP (1-Methyl-2-pyrrolidinone) was diluted to DI water by a 45:55 mL ratio. The weight of NMP/DI water composition was measured and mixed with 2% weight equivalent of MoS_2 powder. The mixture was sonicated for 20 hours and followed by a

centrifugation at 5000 rpm for 30 minutes. The supernatant was filtered out from the top of the mixture after it rested overnight. The resultant MoS_2 ink was yellowish. The viscosity of our MoS_2 ink was ~3.8 cP, which is suitable for inkjet printing. The kinetics of drop formation of MoS_2 was captured by the fiducial camera of the Dimatix printer.

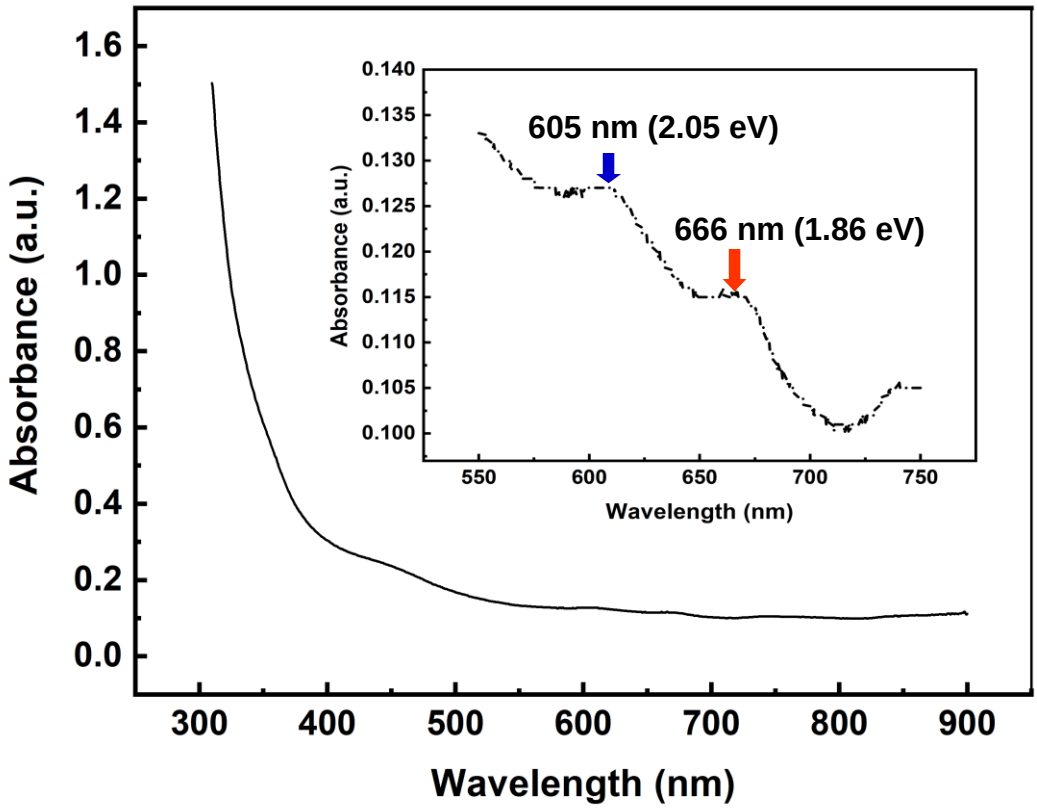

Figure 20. Absorbance spectra of MoS_2 ink.

Figure 20 shows the optical absorbance spectra for as-prepared MoS_2 ink. This absorbance spectrum complies with the previously reported MoS_2 absorbance spectra [36]. The measurements were carried out with a Shimadzu UV-2501 spectrophotometer. For MoS_2 presence in dispersion, two characteristic peaks appear at around 600 and 672 nm wavelength respectively [32]. Two excitonic absorption peaks at 605 and 666 nm are observed, which arise from the k-points of the Brillouin zone in MoS_2 nanosheets. The

peak at 666 nm corresponds to the lowest optical band-gap of 1.86 eV for MoS_2 nanosheets, which is higher than the bulk MoS_2 band-gap of 1.3 eV [45]. The extinction coefficient of MoS_2 at 672 nm wavelength is ~ α_{660} = 3400 mL/(mg.m) [36]. Using the Beer-Lambert law at 672 nm, the calculated final MoS_2 concentration is ~ 0.1 mg/mL.

3.6. Barium Titanate Ink Preparation and Characterization

The barium titanate ($BaTiO_3$) ink was developed utilizing a high-k dielectric nanopowder in conjunction with a printable polymer dielectric. The dielectric ink includes 20% by weight of $BaTiO_3$ nanoparticles, 1 % by weight of the Triton X-100, 14.5 % by weight of Cyclopentanone, and 64.5 % by weight of SU8 2005. The $BaTiO_3$ cubic nanoparticles of 50 nm with dielectric constant 500 to 3000 were used as the high-k dielectric material [46]. The SU8 2005 is a photoresist polymer ($k \sim 3.2$) which was used as the key solvent in the ink. It helps to print a thin layer of dielectric in a printing pass. Triton X-100 in a nonionic surfactant that helps the powder to dissolve in SU8 and reduces the surface tension of SU8 for better printing. The viscosity of SU8 2005 is comparatively higher (45 mPa s) for the Fujifilm Dimatix printer (3 to 20 mPa s). The addition of high weight percentage of $BaTiO_3$ nanoparticles raises the viscosity further. A volatile organic compound Cyclopentanone (viscosity ~ 1.29 mPa s) was added to reduce the viscosity of the solution. The $BaTiO_3$ powder, SU8 2005, Triton X-100, and cyclopentanone were purchased from US Research Nano Materials Inc., MicorChem, and Sigma-Aldrich respectively. For ink preparation, SU8 2005, Cyclopentanone, and Triton X-100 were mixed together and sonicated for 4 hours. The $BaTiO_3$ nanoparticles are then added to the mixture and the composition was sonicated for an additional 6 hours. The resultant mixture was left untouched for one day to form a stable dispersion. The ink was

collected from the suspension, leaving the residue of thick powders at the bottom of the bottle [47].

For curing, the printed layers are first heated at 100 ^{o}C for 20 minutes to evaporate cyclopentanone followed by another 30 minutes of heating at 230 ^{o}C. An average thickness of ~1 µm was measured for single printing pass using KLA Tencor p7 surface profilometer. For robust control of drain current through electric field effect, a thin gate dielectric with high dielectric constant is required.

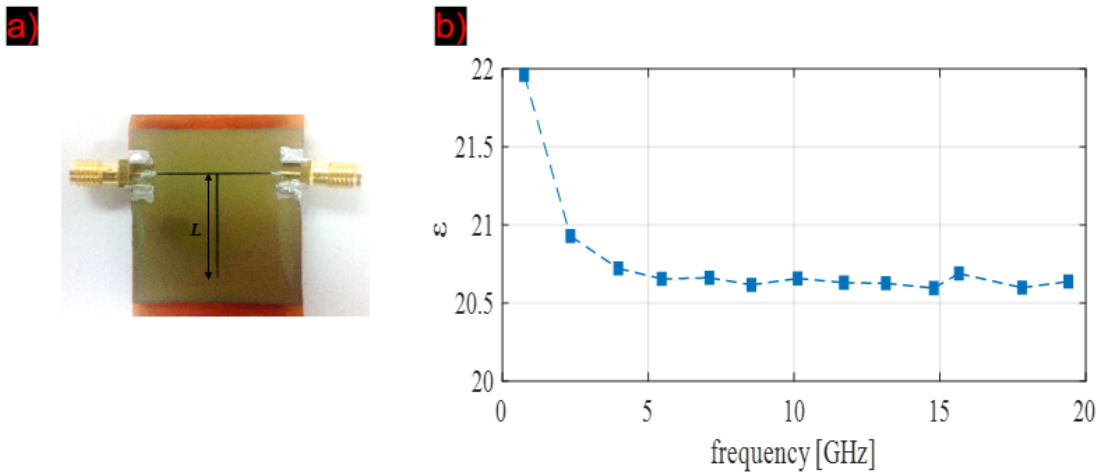

Figure 21. a) Printed T-resonator on Kapton, b) Measured dielectric constant of the printed $BaTiO_3$ using T-resonator.

The effective dielectric constant of the printed dielectric was measured with a T-shape microstrip line resonator as shown in figure 21a [48]. The length of the stub (L) and dielectric constant of the substrate will determine the resonant frequencies. The stub length L, number of harmonic n, velocity of light in air c, f_1 is the fundamental frequency, $f_n = nf_1$ is the resonance frequency of n-th harmonic, ε_{eff} is the effective epsilon of the substrate can be related by following relation:

$$L = \frac{nc}{4 f_n \sqrt{\varepsilon_{eff}}} \qquad (1)$$

The relation between ε_{eff} and bulk permittivity (ε) of the substrate dielectric can be seen in reference 48. To design the T-resonator, an initial guess of the dielectric constant should be considered. Then, the first resonant frequency should be designed based on the desired characterization frequency range. A small f_1 can provide more samples over frequency, but this leads to a longer stub. Figure 21a shows the printed T-resonator with ε_{eff} =9 as an initial guess (after some tries regarding possible stub width and substrate thickness) which leads to L = 25 mm and f_1=1 GHz. The width of microstrip lines is 370 μm based on measurements after fabrication and curing.

To print the T-resonator, first 12 layers of silver ink were printed on a Kapton substrate (brown layer) as the ground plane. The ground plane cannot be seen in figure 21a because it is covered by the dielectric white layer. After curing the silver ink, multiple prints and curing are done to achieve a 96 μm thick film of the dielectric ink as the substrate of T-resonator. The microstrip lines are printed using the same silver ink. Finally, coaxial connectors are soldered to the sample using silver epoxy.

Two ports of an Agilent network analyzer N5230A are connected to SMA coaxial connectors and the S_{12} of the T-resonator is measured from 20 MHz to 20 GHz. Based on the measurement results, the first resonance frequency is observed at 0.7459 GHz. The odd harmonics of f_1 can be seen in the S_{12} measurement, with the ratio of the high order resonance slightly deviating from odd numbers over frequency. So, based on equation (1), the ε_{eff} and then ε can be calculated at resonance frequencies. Figure 21b shows the results of ink epsilon versus frequency. This shows that the ink can provide a high dielectric constant over a wide range of frequencies [48].

IV. DEVICE FABRICATION AND CHARACTERIZATION

4.1. Introduction

The development of all inkjet transistors with 2D channel materials can open a new venue for research. In this thesis, the Fujifilm Dimatix inkjet printer is used for fabricating transistors onto glass substrates. It is a non-contact printing technology where droplets of ink are jetted from a small aperture directly to a specified position to create a pattern. The printer specifications also support printing FET for this research.

4.2. NDG Transistor Fabrication and Characterization

The transistors themselves are all inkjet-printed on the glass substrate without involving any photolithography patterning or surface pretreatment steps. The TFTs are top-gated, consisting of the source and drain electrodes, a channel, and a dielectric layer. Figure 22 shows the schematic structure of an NDG transistor. The design consists of three metal contacts such as source, drain and gate terminals. The source and drain terminals are separated by a carrier transport layer. The transport layer is separated from the gate contact by a dielectric. The electric field propagates through the dielectric and controls the number of carriers in the channel region. A 2D device pattern was created in AutoCAD where the design-layout represents different parts of the transistor. The design pattern was converted into a printable version of the Fujifilm Dimatix printer with ACE 300 software.

Table 2 summarizes the material selections, printing and curing conditions for the printed transistors. The design has four layers in total. The substrate was taken out from the platen for curing after each layer printing. An optical image of final device is displayed in Figure 23. As silver nanoparticle ink is a highly conductive ink (Novacentrix

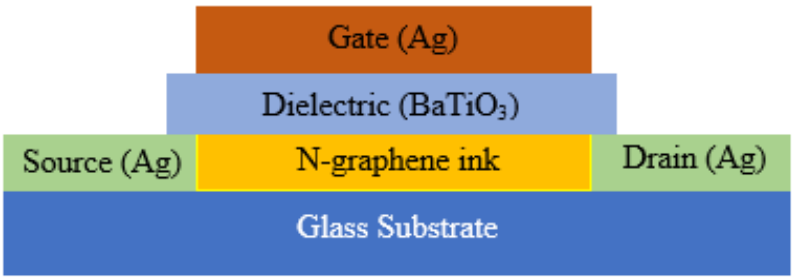

Figure 22. Schematic of top-gated NDG Transistor.

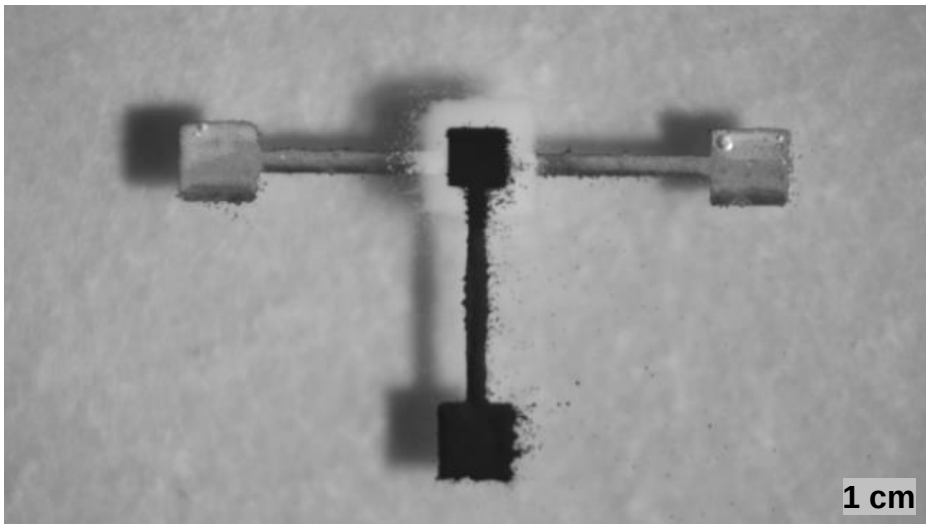

Figure 23. Optical image of final NDG transistor.

Table 2. Printing steps along with candidate materials.

Steps	Layer Name	Material	Designed Thickness	Curing Condition
1	Source / Drain	Silver (Ag)	500 nm	150°C @ 30 min
2	Channel	N-Graphene, MoS_2	100 nm for NDG, 5 nm for MoS_2	NDG – 375°C @ 30min MoS_2 – 100°C @60min
3	Dielectric	$BaTiO_3$	2 µm	100°C @ 20 min, and 230°C @ 30 min
4	Gate	Silver (Ag)	500 nm	120°C @ 60 min

Metalon® JS-B40G), it is used to print source, drain, and gate terminals. As the very first layer, source and drain electrodes were printed on the glass substrate in a printing pass. The separation between source and drain electrodes, i.e. the channel length (L) is ~80 µm. The annealed silver contacts deposited uniformly with an average thickness of 0.50 µm. For NDG transistor, a channel of ~100 nm thickness was created with 40 printing repetitions to ensure the availability of NDG nanosheets on the top surface of the NDG thin films. The channel layer has some overlapping with source and drain contacts to avoid discontinuity in the structure. The $BaTiO_3$ dielectric of 2 µm was created in 2 printing passes to cover the channel region. Finally, the silver gate electrode was printed

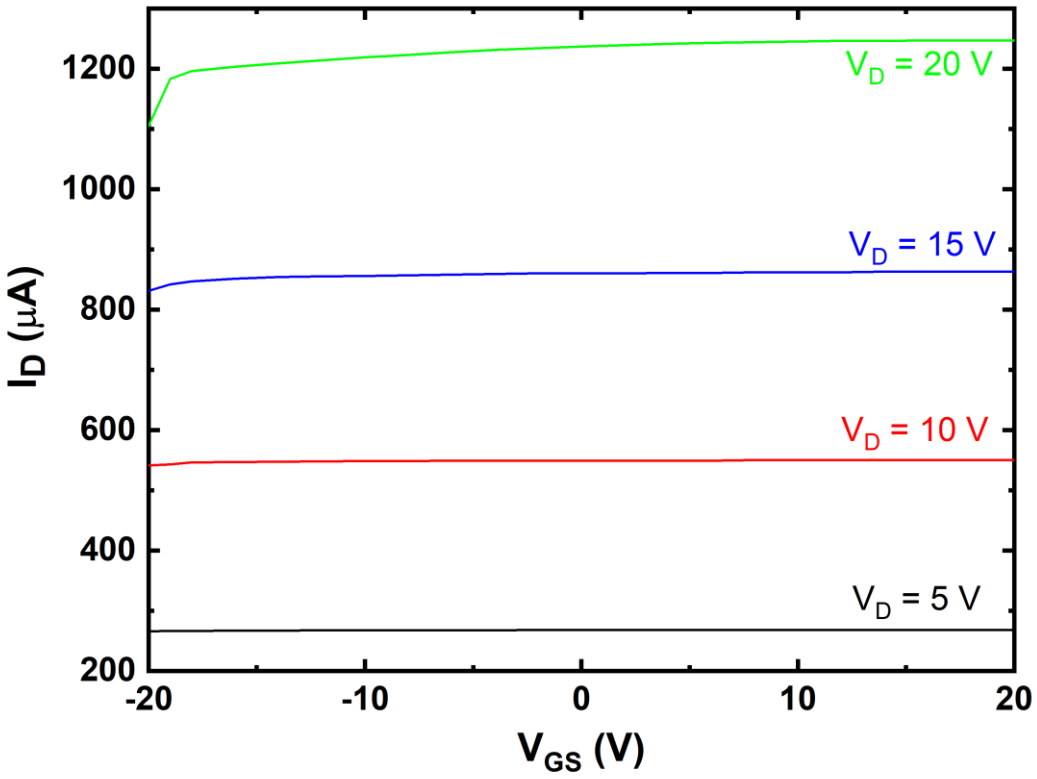

Figure 24. Transfer characteristics of the NDG transistor.

on top of the dielectric layer. The top-illumination on the device causes the shadow on the glass substrate background. The source/drain and gate contacts are looking dissimilar

due to the different curing temperatures. Note that neither surface pretreatments on the substrate before printing, nor passivation, were performed after the printing of the transistor.

Transfer characteristics of the NDG transistor are shown in Figure 24. The gate voltages are changed from -20 to +20 V. The transfer characteristics are measured at V_D = 5, 10, 15, and 20 V respectively, using a Keysight B1500A semiconductor device analyzer. The drain current increases as the V_{GS} changes from negative to positive, which confirms the n-type doping in NDG nanosheets due to nitrogen doping. However, the drain current does not change significantly over a wide range of gate modulation. For example at V_D = 20V, the drain current changes from 1105 to 1247 µA in the given gate voltage range. This suggests a negligible amount of band-gap opening in the nanosheets as well as n-type doping. The current on/off ratio can be calculated from the transfer characteristics and it is the ratio of maximum to minimum drain current for a specific V_D. At V_D = 20, the on/off ratio of the NDG is ~ 1.13. This on/off ratio is comparable to other inkjet-printed graphene TFTs, but not suitable for transistor switches [10]. The effective mobility µ can be derived from the slope of the transfer characteristics using $\mu = (L*g_m/W*C_{ox}*V_d)$, where L (80 µm) and W (200 µm) are channel length and width, C_{ox} is the gate capacitance (≈ 9.07 nF/cm^2), and $g_m = dI_d/dV_g$ is the transconductance (3.55 µS). The estimated device mobility is ≈ 7.85 cm^2/V.s. The output curve of the NDG transistor is plotted in Figure 25. The drain currents were measured in V_{GS} = -20, -10, 0, 10, and 20 V respectively. Still the linear I_D - V_D curves were not distinguishable for various gate voltages, i.e. the field effect in the output curves were not apparent. Therefore, a linear I_D-V_D curve for V_{GS} = 10 V is displayed in the output characteristics.

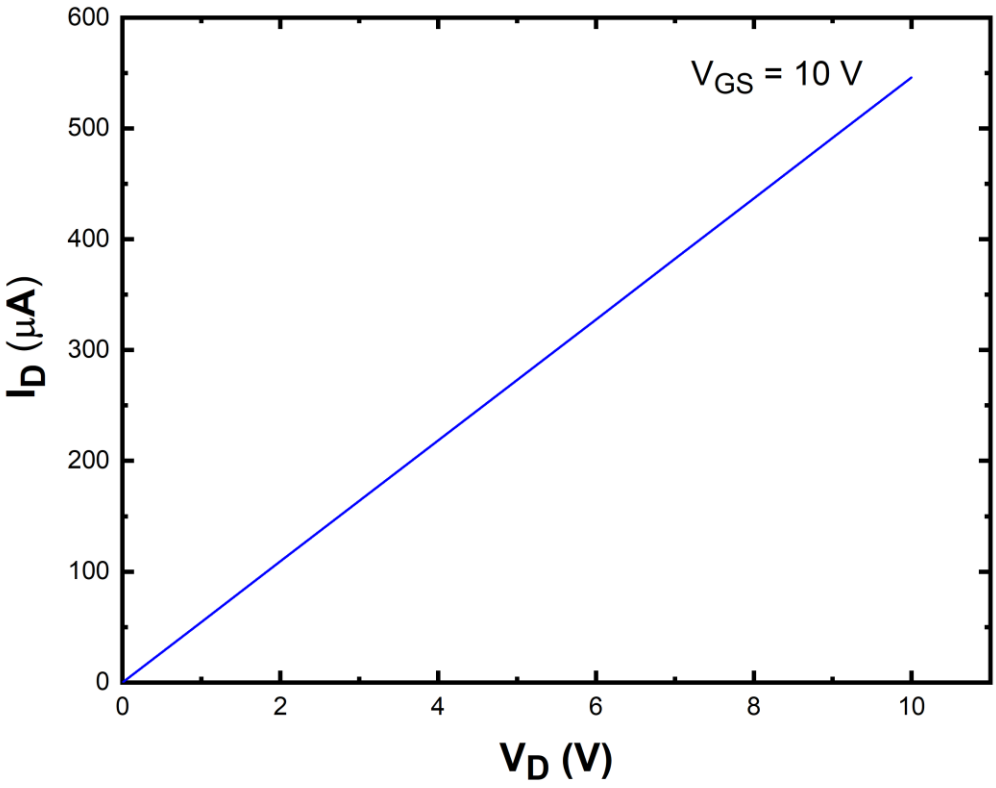

Figure 25. Output characteristics of the NDG transistor.

4.3. NDG and Molybdenum Disulfide Heterostructures

Based on our primary hypothesis, NDG TFTs should have higher current on/off ratios than those of graphene TFTs. But their on/off ratios are in the same scale. So, we must try all the possible ways to improve the current ratio. The MoS_2 dispersions produced by LPE have the optical band-gap ranges from ~1.8 eV to 1.3 eV [38]. But, the MoS_2 percolation networks behave like an open circuit for a distance greater than 28 μm [32]. It is possible to create a heterostructure assembly of inkjet-printed 2D materials with novel properties [7]. Therefore, we created and optimized the heterostructures of inkjet printed NDG and MoS_2 materials. For 10 printing passes of NDG ink, a printing pass of semiconducting MoS_2 ink was performed. Figure 26 shows the SEM images of 20 layers

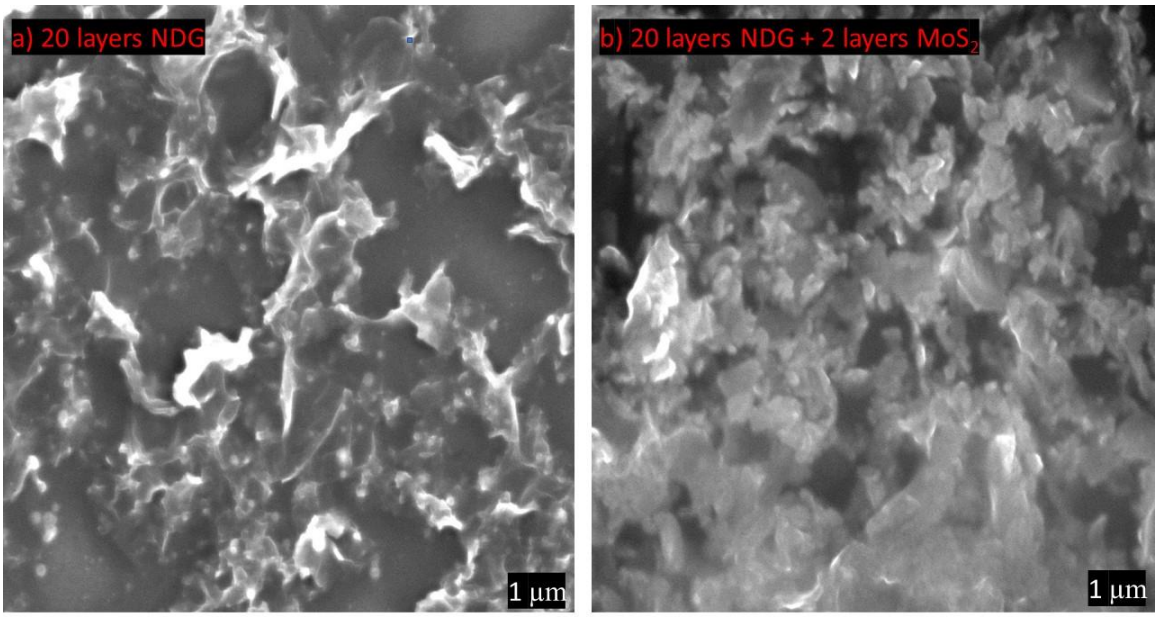

Figure 26. a) SEM image of 20 layers NDG, b) SEM image of NDG and MoS_2 heterostructure.

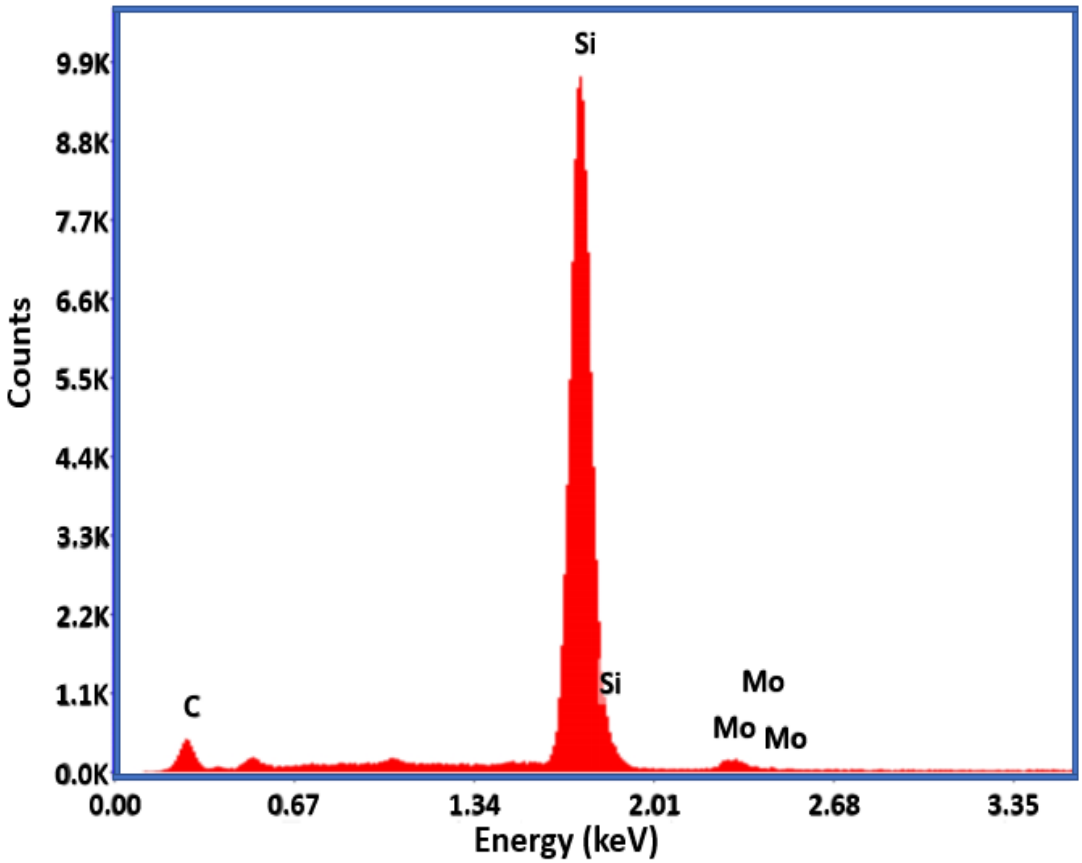

Figure 27. EDS spectrum of NDG/MoS_2 heterostructure on Si substrate.

of NDG before and after being electrochemically doped with MoS_2 on a Si substrate. The protruding NDG nanosheets of Figure 26a turned into a fracture-like structure with two additional MoS_2 printing passes. The change in surface morphology confirms the incorporation of MoS_2 into NDG nanosheets. Hence, this hybrid structure is known as NDG-MoS_2 heterostructure. The EDS spectrum of the NDG-MoS_2 as presented in Figure 27 is obtained for further verification. The EDS analysis shows that the elements in the heterostructure are carbon (C), molybdenum (Mo), and silicon (Si). The EDS spectrum confirms the existence of Mo and C on Si substrate. The weight percentage (weight %) of C and Mo components are 27.26 and 3.30 in the films respectively. The energy dispersive detector could not detect nitrogen (N) and sulfur (S) elements in the sample. The reason for the absence of N and S is that their weight percentage in our sample lies below the detection limit of EDS analysis. No other elements or impurities are observed. The EDS spectra are measured for two additional samples. The weight percentages of Mo and C are consistent with the first measurement. The elements, weight, atomic, and error percentages are outlined in Table -3.

Table 3. Summary of EDS spectra.

Sample Number	Element	Weight %	Atomic %	Error %
Sample 1	C K	27.26	47.51	12.52
	Si K	69.44	51.77	2.54
	Mo L	3.30	0.72	15.61
Sample 2	C K	27.38	47.57	12.62
	Si K	69.73	51.81	2.55
	Mo L	2.89	0.63	14.72
Sample 3	C K	26.66	46.79	12.65

	Si K	69.86	52.44	2.56
	Mo L	3.49	0.77	16.31

4.4. NDG-MoS_2 Transistor Fabrication and Characterization

All inkjet printed TFTs with NDG-MoS_2 channel were fabricated in quest of high on/off ratio transistors. Figure 28 shows the schematic of the top-gated NDG-MoS_2 heterostructure transistor. The TFTs are fabricated following the same way as discussed in Section 4.2 except the channel region. The channel length is ~ 80 µm. For channel region, a percolation network of ~100 nm NDG was created with 40 printing passes followed by an MoS_2 printing repeating 4 times.

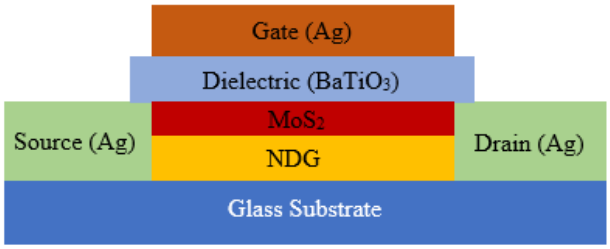

Figure 28. Schematic of top-gated NDG-MoS_2 heterostructure TFT.

Figure 29 shows the non-linear transfer curve of the NDG-MoS_2 transistor at V_D = -2 V. The current-voltage measurements were performed using Keysight B1500A semiconductor device analyzer. The applied gate voltage changed from -20 to 10V. The device did not saturate within our measurement range. The I_D increases as the gate voltage goes from positive to negative, which suggests that the NDG-MoS_2 heterostructure creates a p-type transport layer as shown in Figure 29. The current on/off ratio is the ratio of maximum to minimum drain current in a transfer curve for a specific drain voltage. A current on/off ratio of 1200 is calculated at $V_D = -2$ V from the transfer curve This is the highest on/off ratio reported to date for inkjet printed 2D materials

transistor. The device mobility was ~ 0.01 cm^2/V.s. which is comparable with liquid exfoliated MoS_2 based TFTs [36]. Moreover, the device has a good-off state.

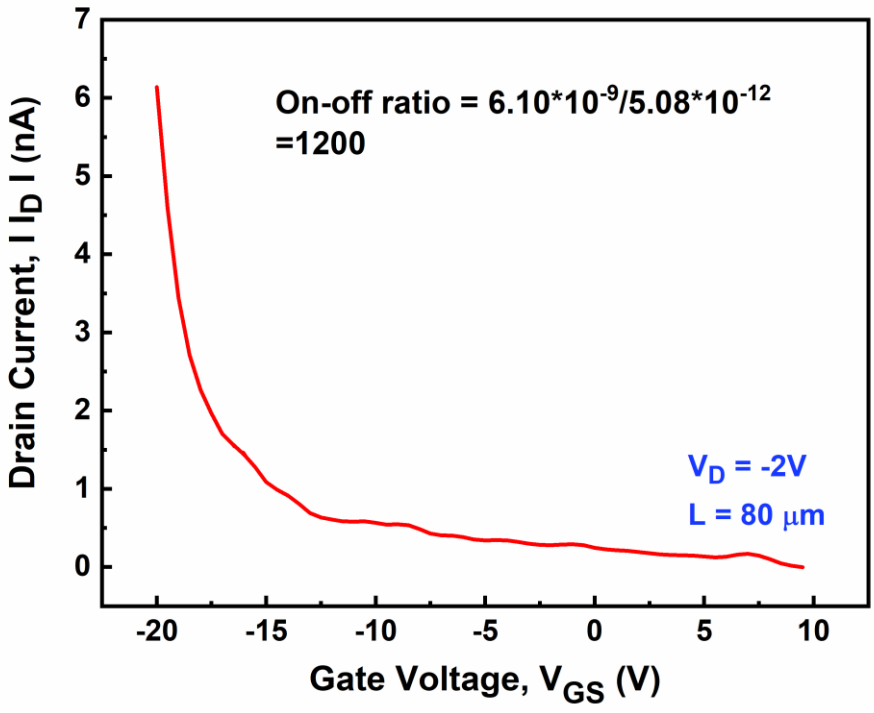

Figure 29. Transfer curve of NDG-MoS_2 transistor.

Figure 30 shows the output characteristics of the NDG/MoS_2 transistor at gate voltage sweep from 10 to -20 V respectively. The gate modulation is obvious in the output curves. The output characteristics show weak saturation. The I_D-V_D curves did not have any Schottky behavior, which was reported earlier for an MoS_2 TFT [34]. The transfer and output characteristics of the device exhibit p-type behaviors. Earlier p-type transistor behavior was reported for inkjet printed MoS_2 transistor [32]. However, for a channel length of 80 µm, printed MoS_2 percolation networks act like an open circuit [32]. Therefore, we believe the p-type behavior of our device is due to both MoS_2 and NDG although nitrogen dopants induce n-type doping in graphene. Additionally, the top layer in the NDG-MoS_2 heterostructure channel was MoS_2, which is a semiconductor. It is

reasonable to believe that MoS_2 had the major contribution to the drain current conduction. The high on/off ratio reflected the existence of a semiconducting percolation network in the channel region.

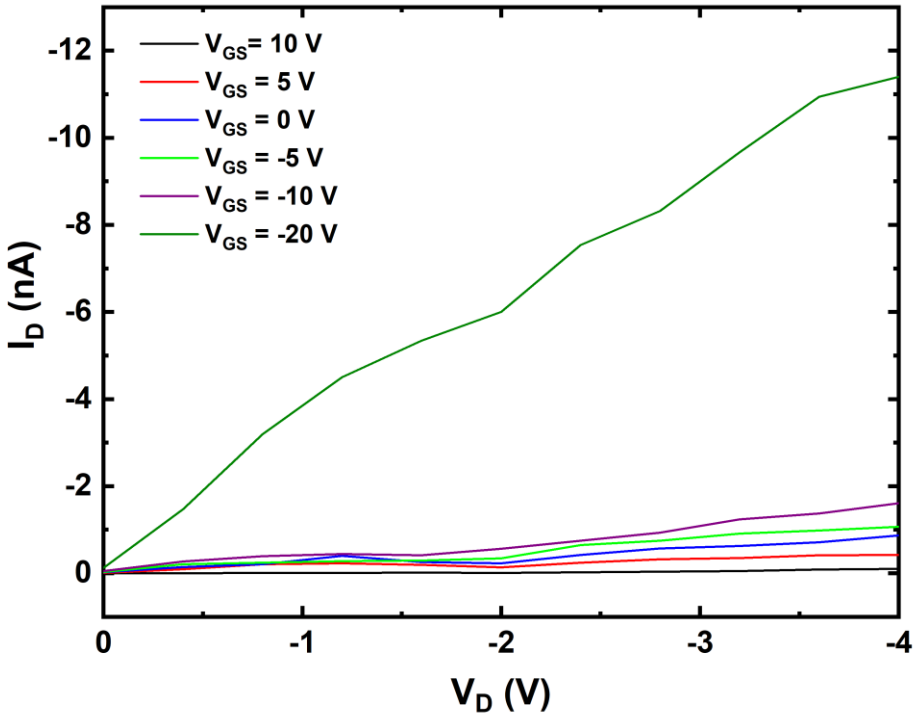

Figure 30. Output characteristics of NDG-MoS_2 transistor.

Table 4 compares the current ratios and synthesis methods of 2D material TFTs. The comparison is also depicted with a bar graph in Figure 31. The LPE and IJP stand for liquid phase exfoliation, and inkjet printing respectively. The current on/off ratio of an NDG-MoS_2 transistor is very high compared to the reported IJP and LPE deposited 2D material transistors. To our best knowledge, NDG-MoS_2 transistor has the highest on/off ratio compared to its peers. For the TFTs of reference 38, they sprayed the dielectric and the measurements were carried out under ultra-high vacuum and low temperature. These devices were not all inkjet printed. 100% inkjet-printed devices do not require photolithography patterning, or surface pretreatment steps, and a complete device can be

fabricated with one inkjet printer. In summary, we developed a 2D materials based, 100% inkjet-printed, high current on/off ratio transistor.

Table 4. Comparison of on/off ratios of 2D materials TFTs				
Reference	On/Off Ratio	Material	Deposition	100% inkjet printed
7	2.5	Graphene	IJP	Yes
8	10	Graphene	IJP	No
10	1.2	Graphene	IJP	No
32	3 ~ 6	MoS_2	IJP	No
34	3 ~ 4	MoS_2	LPE	No
36	<10	MoS_2	LPE	No
37	10	MoS_2	IJP	No
38	25	WSe_2	IJP	No
Our work	1200	NDG-MoS_2	IJP	Yes

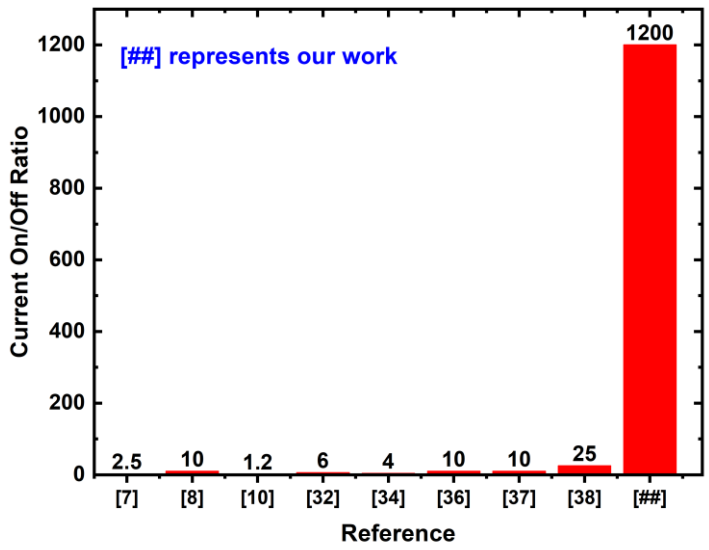

Figure 31. Comparison of previously reported current on/off ratios.

V. CONCLUSIONS

The primary contribution of this research is to make stable dispersions of NDG nanosheets for inkjet printing, understand the thin film and transistor properties through the experimental characterizations. Moreover, NDG ink can be used as an electrocatalyst, in sensors, lithium-ion batteries, and supercapacitors. The doped graphene transistors behave like typical graphene TFTs and have low current on/off ratio. We devised a way to improve the current on/off ratio of transistors enormously with 2D channel materials at room temperature. The devices are fully inkjet-printed without any involvement of Cleanroom facility. The devices displayed controllable field effect over a large area compared to the printed MoS_2 transistors fabricated with inter-digitated electrodes (channel length ~ 1μm). The transistor has relatively low off current, i.e. good off-state. Based on the test results of DC analysis of the device, the current on/off ratio of 1200 is reported in this thesis, which is the highest reported so far in the literature.

Although we have demonstrated a high current on/off ratio transistor, a significant work remains to be done in this domain. The on-current of the device is in nanoampere range. The mobility is low and comparable to LPE MoS_2, however, for practical devices, it needs to be improved significantly. For low voltage operation of the devices, a thin layer of dielectric or a high-*k* dielectric can be used. As the on/off ratio improved by p-type MoS_2 nanosheets, it is possible to take advantage of p-type doped graphene, for example, boron-doped graphene nanosheets to increase charge carriers in the channel region. The device channel length and width must be small for low channel resistance to increase on-current. With such improvements, we believe 2D material transistors can be

parallel to other 100% inkjet printed transistors in terms of performance and ease of fabrication.

APPENDIX SECTION

Table 5. Data table for Raman measurements.

Observation Number	Number of printing passes	D Peak Position (cm^{-1})	G Peak Position (cm^{-1})	2D peak position (cm^{-1})	I_D (a.u.)	I_G (a.u.)	I_{2D} (a.u.)	I_D / I_G	I_{2D} / I_G
1	2	1350	1586	2690	346.907	988.156	228.163	0.351	0.230
2		1347	1586	2682	622.268	1712.24	48.092	0.362	0.028
3		1352	1587	2698	642.474	1342.88	66.7688	0.478	0.049
4		1351	1583	2682	341.001	824.549	61.9599	0.413	0.075
1	5	1368	1588	2693	675.994	805.079	118.872	0.839	0.147
2		1348	1590	2692	1002.75	2428.2	70.0268	0.412	0.028
3		1339	1580	2666	727.288	2815.1	164.017	0.258	0.058
4		1348	1588	2708	1269.83	1317.21	113.57	0.964	0.086
1	10	1345	1568	2693	1569.52	2468.49	397.929	0.635	0.161
2		1345.38	1589	2711	1438.95	1587.01	164.004	0.906	0.103
3		1344	1583	2686	1420.34	1450.28	247.944	0.979	0.170
4		1349	1594	2686	1620.22	1729.49	165.427	0.936	0.095
1	Powder	1342	1577	2675	266.177	313.886	59.9369	0.848	0.190
2		1341	1575	2672	263.555	250.813	50.5023	1.050	0.201
3		1333	1572	2667	372.381	338.206	70.9321	1.101	0.209
4		1341	1569	2680	251.053	271.474	74.2074	0.924	0.273

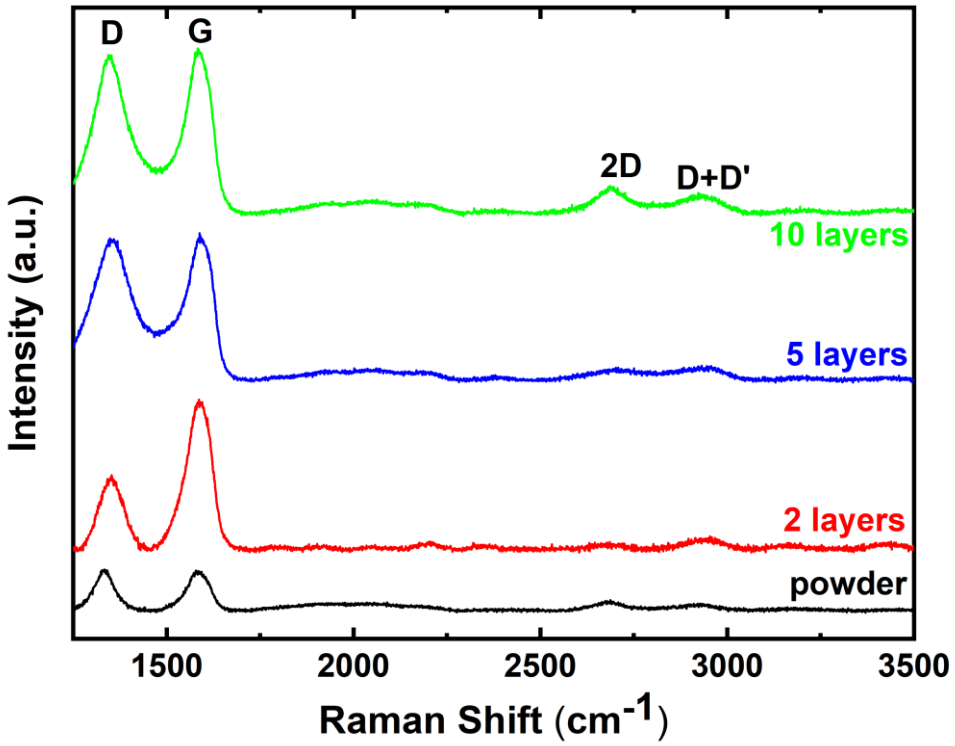

Figure 32. Raman spectra of the printed NDG layers.

LITERATURE CITED

[1] Y. Kervran et al., “Silicon: A flexible material for bendable electronics and sensors,” in SBMicro 2016 - 31st Symposium on Microelectronics Technology and Devices: Chip on the Mountains, co-located 29th SBCCI - Circuits and Systems Design, 6th WCAS - IC Design Cases, 1st INSCIT - Electronic Instrumentation and 16th SForum - Undergraduate-Student Forum, 2016.

[2] Das, R.; Ghaffarzadeh, K.; He, X.; “Printed, Organic & Flexible Electronics Forecasts, Players & Opportunities 2017-2027,” IDTechEx report, 2017.

[3] R.-P. Xu, Y.-Q. Li, and J.-X. Tang, “Recent advances in flexible organic light-emitting diodes,” J. Mater. Chem. C, vol. 4, no. 39, pp. 9116–9142, 2016.

[4] G. K. J. Chen and J. Chen, “Flexible displays: Flexible AMOLED manufacturing,” in Handbook of Visual Display Technology, 2016, pp. 1359–1376.

[5] P. M. Grubb, H. Subbaraman, S. Park, D. Akinwande, and R. T. Chen, “Inkjet printing of high performance transistors with micron order chemically set gaps,” Sci. Rep., vol. 7, no. 1, 2017.

[6] B. Huber, P. B. Popp, M. Kaiser, A. Ruediger, and C. Schindler, “Fully inkjet printed flexible resistive memory,” Appl. Phys. Lett., vol. 110, no. 14, 2017.

[7] T. Carey et al., “Fully inkjet-printed two-dimensional material field-effect heterojunctions for wearable and textile electronics,” Nat. Commun., vol. 8, no. 1, 2017.

[8] F. Torrisi et al., “Inkjet-printed graphene electronics,” ACS Nano, vol. 6, no. 4, pp. 2992–3006, 2012.

[9] A. Kamyshny and S. Magdassi, “Conductive nanomaterials for printed electronics,” Small, vol. 10, no. 17. pp. 3515–3535, 2014.

[10] J. Li, F. Ye, S. Vaziri, M. Muhammed, M. C. Lemme, and M. Östling, “Efficient inkjet printing of graphene,” Adv. Mater., vol. 25, no. 29, pp. 3985–3992, 2013.

[11] P. Calvert, “Inkjet printing for materials and devices,” Chemistry of Materials, vol. 13, no. 10. pp. 3299–3305, 2001.

[12] B. Derby, “Additive Manufacture of Ceramics Components by Inkjet Printing,” Engineering, vol. 1, no. 1, pp. 113–123, 2015.

[13] Dimatix Materials Printer DMP-2800 Series User Manual. V. 1.5.0.1.

[14] Mattana Giorgio et al., “Inkjet-Printing: A New Fabrication Technology for Organic Transistors,” Adv. Mater. Technol., vol. 2, pp. 1700063, 2017.

[15] L. Feng, C. Jiang, H. Ma, X. Guo, and A. Nathan, “All ink-jet printed low-voltage organic field-effect transistors on flexible substrate,” Org. Electron., vol. 38, pp. 186–192, 2016.

[16] S. Jung et al., “All-inkjet-printed, all-air-processed solar cells,” Adv. Energy Mater., vol. 4, no. 14, 2014.

[17] B. Huber, P. B. Popp, M. Kaiser, A. Ruediger, and C. Schindler, “Fully inkjet printed flexible resistive memory,” Appl. Phys. Lett., vol. 110, no. 14, 2017.

[18] H. He, L. Sydänheimo, J. Virkki, and L. Ukkonen, “Experimental Study on Inkjet-Printed Passive UHF RFID Tags on Versatile Paper-Based Substrates,” Int. J. Antennas Propag., vol. 2016, 2016.

[19] A. K. Geim and K. S. Novoselov, “The rise of graphene,” Nat. Mater., vol. 6, no. 3, pp. 183–191, 2007.

[20] X. Li and H. Zhu, “Two-dimensional MoS_2: Properties, preparation, and applications,” J. Mater., vol. 1, no. 1, pp. 33–44, 2015.

[21] Xia et al., “Graphene Field-Effect Transistors with High On/Off Current Ratio and Large Transport Band Gap at Room Temperature,” Nano Lett., vol. 10, no. 2, pp. 715-718, 2010.

[22] F. Schwierz, “Graphene Transistors,” Nat. Nanotechnol. vol. 5, pp. 487–496, 2010.

[23] M. Y. Han, B. Özyilmaz, Y. Zhang, and P. Kim, “Energy band-gap engineering of graphene nanoribbons,” Phys. Rev. Lett., vol. 98, no. 20, 2007.

[24] S. Y. Zhou et al., “Substrate-induced bandgap opening in epitaxial graphene,” Nat. Mater., vol. 6, no. 10, pp. 770–775, 2007.

[25] E. V. Castro et al., “Biased bilayer graphene: Semiconductor with a gap tunable by the electric field effect,” Phys. Rev. Lett., vol. 99, no. 21, 2007.

[26] J. Warmuth et al., “Band-gap engineering by Bi intercalation of graphene on Ir(111),” Phys. Rev. B, vol. 93, no. 16, 2016.

[27] S. Mukherjee and T. P. Kaloni, “Electronic properties of boron- and nitrogen-doped graphene: A first principles study,” J. Nanoparticle Res., vol. 14, no. 8, 2012.

[28] J. A. Lawlor and M. S. Ferreira, “Sublattice asymmetry of impurity doping in graphene: A review,” Beilstein Journal of Nanotechnology, vol. 5, no. 1. pp. 1210–1217, 2014.

[29] W. Zhang et al., “Opening an electrical band gap of bilayer graphene with molecular doping,” ACS Nano, vol. 5, no. 9, pp. 7517–7524, 2011.

[30] C. Jeon et al., “Opening and reversible control of a wide energy gap in uniform monolayer graphene,” Sci. Rep., vol. 3, 2013.

[31] A. Ramasubramaniam, D. Naveh, and E. Towe, “Tunable Band Gaps in Bilayer Graphene- BN Heterostructures,” Nano Lett., vol. 11, no. 3, pp. 1070–5, 2011.

[32] J. Li, M. M. Naiini, S. Vaziri, M. C. Lemme, and M. Östling, “Inkjet printing of MoS_2,” Adv. Funct. Mater., vol. 24, no. 41, pp. 6524–6531, 2014.

[33] B. Radisavljevic, A. Radenovic, J. Brivio, V. Giacometti, and A. Kis, “Single-layer MoS_2 transistors,” Nat. Nanotechnol., vol. 6, no. 3, pp. 147–150, 2011.

[34] K. Lee, H. Y. Kim, M. Lotya, J. N. Coleman, G. T. Kim, and G. S. Duesberg, “Electrical characteristics of molybdenum disulfide flakes produced by liquid exfoliation,” Advanced Materials, vol. 23, no. 36. pp. 4178–4182, 2011.

[35] T. Carey et al., “Fully inkjet-printed two-dimensional material field-effect heterojunctions for wearable and textile electronics,” Nat. Commun., vol. 8, no. 1, 2017.

[36] J. N. Coleman et al., “Two-dimensional nanosheets produced by liquid exfoliation of layered materials,” Science (80-.)., vol. 331, no. 6017, pp. 568–571, 2011.

[37] Q. He et al., “Fabrication of flexible MoS_2 thin-film transistor arrays for practical gas-sensing applications,” Small, vol. 8, no. 19, pp. 2994–2999, 2012.

[38] A. G. Kelly et al., “All-printed thin-film transistors from networks of liquid-exfoliated nanosheets,” Science (80-.)., vol. 356, no. 6333, pp. 69–73, 2017.

[39] A. C. Ferrari et al., “Raman spectrum of graphene and graphene layers,” Phys. Rev. Lett., vol. 97, no. 18, 2006.

[40] Z. Zafar et al., “Evolution of Raman spectra in nitrogen doped graphene,” Carbon N. Y., vol. 61, pp. 57–62, 2013.

[41] P. Venezuela, M. Lazzeri, and F. Mauri, “Theory of double-resonant Raman spectra in graphene: Intensity and line shape of defect-induced and two-phonon bands,” Phys. Rev. B - Condens. Matter Mater. Phys., vol. 84, no. 3, 2011.

[42] Y.-F. Lu et al., “Nitrogen-Doped Graphene Sheets Grown by Chemical Vapor Deposition: Synthesis and Influence of Nitrogen Impurities on Carrier Transport,” ACS Nano, vol. 7, no. 8, pp. 6522–6532, 2013.

[43] Y. Hernandez et al., “High-yield production of graphene by liquid-phase exfoliation of graphite,” Nat. Nanotechnol., vol. 3, no. 9, pp. 563–568, 2008.

[44] M. U. Jewel, M. S. Mahmud, A. Zakhidov, and M.Y. Chen, “Low Temperature Atomic Layer Deposition of Zirconium Oxide for Inkjet Printed Transistor Applications.” [unpublished]

[45] A. K. Mishra, K. V. Lakshmi, and L. Huang, “Eco-friendly synthesis of metal dichalcogenides nanosheets and their environmental remediation potential driven by visible light,” Sci. Rep., vol. 5, 2015.

[46] V. Petrovsky, T. Petrovsky, S. Kamlapurkar, and F. Dogan, “Dielectric constant of barium titanate powders near curie temperature,” J. Am. Ceram. Soc., vol. 91, no. 11, pp. 3590–3592, 2008.

[47] M. U. Jewel, F. Mokhtari-Koushyar, and M.Y. Chen, “All Inkjet-Printed High On/Off Ratio Two-Dimensional Materials Field Effect Transistor,” The 18th IEEE International Conference on Nanotechnology, Cork, Ireland 2018 (accepted).

[48] K.-P. Latti, M. Kettunen, J.-P. Strom, and P. Silventoinen, “A review of microstrip T-resonator method in determining the dielectric properties of printed circuit board materials,” IEEE Trans. Instrum. Meas., vol. 56, pp. 1845-1850, 2007.